bioRxiv preprint doi: https://doi.org/10.1101/309245; this version posted April 30, 2018. The copyright holder for this preprint (which was not certified by peer review) is the author/funder. All rights reserved. No reuse allowed without permission.

Functional recruitment of dynamin requires multimeric interactions for efficient endocytosis

Authors: Morgane ROSENDALE[1,2,3,+], Thi Nhu Ngoc VAN[1,2,4,+], Dolors GRILLO-BOSCH[1,2,+], Isabel GAUTHEREAU[1,2], Stéphane CLAVEROL[5], Daniel CHOQUET[1,2,6], Matthieu SAINLOS[1,2] & David PERRAIS[1,2,*]

Affiliations:
[1]University of Bordeaux and [2]CNRS, Interdisciplinary Institute for Neuroscience, UMR 5297, F-33000 Bordeaux, France.

[3]Present address: Brain Science Institute, RIKEN, Wako, Saitama 351-0198, Japan

[4]Present address: Sys2diag Montpellier, France

[5]Proteome Platform, Functional Genomic Center of Bordeaux, University of Bordeaux, Bordeaux, France

[6]Bordeaux Imaging Center, UMS 3420 CNRS, Université de Bordeaux, US 4 INSERM, F-33000, Bordeaux, France

[+] These authors contributed equally to this work, [*]Lead author

Correspondence: Correspondence related to cell assays to D.P. (david.perrais@u-bordeaux.fr). Correspondence related to peptide synthesis and assays to M.S. (matthieu.sainlos@u-bordeaux.fr).

Running title: Multimeric interactions for dynamin recruitment

Keywords: SH3 domain, amphiphysin, TIRF microscopy

Author contributions: M.R., M.S. and D.P. conceived the study and formulated the models. M.R. performed most of the ppH patch clamp experiments and analysed the corresponding data. T.N.N.V. performed most TKO cell experiments and analysed the corresponding data. D.G-B. synthesized and characterized the peptides and performed the peptide pull-down

bioRxiv preprint doi: https://doi.org/10.1101/309245; this version posted April 30, 2018. The copyright holder for this preprint (which was not certified by peer review) is the author/funder. All rights reserved. No reuse allowed without permission.

experiments. I.G. produced and purified the SH3 domains. S.C. performed mass spectrometry data analysis. M.S. performed the SPR experiments and supervised all aspects of biochemical experiments. D.P. wrote the Matlab analysis programs, performed some ppH patch clamp and live cell imaging experiments and analysed the live cell imaging experiments. M.R. and D.P. wrote the manuscript and all the other authors edited the manuscript.

Acknowledgements: We thank Christelle Breillat, Célia Michel and Natacha Retailleau for help with plasmid constructs, Christopher Borcuk for help with Matlab programming, Pascal Desbarats (LaBRI, Bordeaux) for counselling on the SVM for sorting scission events, Sébastien Marais (Bordeaux Imaging Center, part of the France BioImaging national infrastructure ANR-10-INBS-04) for help with the spinning disk confocal microscope. We thank Pietro De Camilli (Yale University) and David Drubin (UC Berkeley) for the gift of cell lines. This work was supported by the Centre National de la Recherche Scientifique (Interface program), the Fondation Recherche Médicale (FRM), the Agence Nationale pour la Recherche (CaPeBlE ANR-12-BSV5-005) to D.P., the FRM, a pre-doctoral fellowship from the University of Bordeaux and a Labex BRAIN fellowship to M.R. and the ERC (advanced grant ADOS) do D.C.

bioRxiv preprint doi: https://doi.org/10.1101/309245; this version posted April 30, 2018. The copyright holder for this preprint (which was not certified by peer review) is the author/funder. All rights reserved. No reuse allowed without permission.

During clathrin mediated endocytosis (CME), membrane scission is achieved by the concerted action of dynamin and its interacting partners[1,2]. The dynamin-mimicking peptide D15 inhibits endocytosis in living cells[3–5] by disrupting the interaction between the proline/arginine-rich domain of dynamin (dynPRD) and the Src-homology domain 3 of amphiphysin (amphSH3). However, the low affinity of D15 for amphSH3 raises a question: how could a weak dynamin-amphiphysin interaction result in the precise spatio-temporal recruitment of dynamin? Here, we propose that oligomerisation increases the avidity of the interaction by bringing multiple binding sites in close proximity. We found that divalent dynPRD-derived peptides bind more strongly than monovalent ones to multimers of amphSH3. Consistently, divalent peptides block endocytosis more effectively than monovalent ones in living cells. Moreover, while a mutant dynamin modified in the D15 motif alone partially rescues endocytosis in dynamin triple knock-out cells, mutations in flanking SH3-binding sites prevent that rescue. Finally, the frequency of endocytic events decreases with hypomorphic rescue mutants but the kinetics of dynamin recruitment is unaffected. This suggests that PRD-SH3 interactions act upstream of dynamin accumulation at the neck of nascent vesicles. We conclude that dynamin drives vesicle scission *via* multivalent interactions *in vivo*.

The dynPRD is a major interaction hub for SH3 domain-containing endocytic accessory proteins[1,6]. Among those, amphiphysin plays a central role in regulating the recruitment of dynamin at CME sites[3,7–10] at a late stage of clathrin coated vesicle (CCV) formation. The amphiphysin specific binding site consists of two overlapping Class-II SH3-binding motifs (PxxPxR) resulting in its characteristic PxRPxR consensus sequence (where P is proline, R is positively charged arginine and x is any amino-acid)[11]. The D15 peptide containing this critical motif has been extensively used to inhibit endocytosis in living cells[3–5,12]. However, its affinity for amphSH3 (K_D ~90 µM)[5] is >1000-fold lower than the reported affinity of the last 44 C-terminal amino-acids of dyn1-PRD (K_D ~25 nM)[13], a peptide sequence we shall name D44 (Figure 1A). We confirmed those reports by directly comparing the affinity values of D15 and D44 with surface plasmon resonance (SPR) assay. We found robust binding of GST-amphSH3 to D44, with an estimated K_D of 572 nM, whereas there was no measureable binding to D15 below 1 µM (Figure 1B). We noted that the D44 sequence displays an additional class-II SH3 binding motif (Figure 1A). Because GST forms dimers[14] as confirmed by size exclusion

bioRxiv preprint doi: https://doi.org/10.1101/309245; this version posted April 30, 2018. The copyright holder for this preprint (which was not certified by peer review) is the author/funder. All rights reserved. No reuse allowed without permission.

chromatography for GST-amphSH3 (Figure 1C), we hypothesised that dimers of GST-amphSH3 could bind simultaneously to the amphiphysin binding motif and this flanking motif, thereby stabilizing the interaction. We thus produced an amphSH3 domain fused with small ubiquitin-like modifier (SUMO), that remains monomeric (Figure 1C), and indeed the affinity gain of D44 over D15 was lost for this domain (102 µM vs 37 µM for D15 and D44, respectively, Figure 1D,E). To rule out any additional effect of the GST tag besides dimerization, we made a multimeric amphSH3 by reacting a biotinylated SUMO-amphSH3 with neutravidin. This Ntr-bSUMO-amphSH3 complex regained high affinity for D44 (17 nM) while D15 did not (Figure 1F). Interestingly, these increases in affinity correspond to slower dissociation rate constants as expected from multivalent interactions.

To further test the divalent binding hypothesis, we designed synthetic ligands that mimic the presence of multiple SH3 binding motifs in dyn1-PRD. These divalent dynamin-derived peptide variants consist of two D15 peptide motifs linked through their N or C termini by a PEG linker (dD15-N and dD15-C: Figure 1A, Supplementary Figure 1). They behaved in a qualitatively similar manner as D44 such that they bound Ntr-bSUMO-amphSH3 and GST-amphSH3 much better than SUMO-amphSH3. For example, dD15-N bound SUMO-SH3, Ntr-bSUMO-amphSH3 and GST-SH3 with K_Ds of 65 µM, 4.5 nM and 509 nM, respectively (Figure 1B-F). To further characterize the functional relevance of the increased valence of those peptides, we performed affinity isolation assays on brain lysates. D15 was unable to pulldown any detectable amount of protein whereas dD15-N isolated a number of proteins, including a clear staining around 70-75 kDa, the awaited molecular weight for amphiphysin (Figure 1G). Moreover, mass spectroscopy analysis showed that the co-precipitated proteins were highly enriched in CME related proteins and in particular known interactors of dynamin (Supplementary Table 2). Our *in vitro* data therefore support the idea that multimerisation of SH3 domains together with the presence of multiple SH3 binding motifs in dynPRD play a role in increasing the avidity of their interaction.

To decipher whether the multimerisation of amphiphysin and other dynamin interaction partners is relevant *in vivo*, we assessed whether the multivalent D44 and divalent peptides exhibited an increased inhibitory activity over the monovalent D15 on CME. We monitored cellular endocytic activity using the pulsed-pH (ppH) assay which detects the formation of single CCVs with a temporal resolution of 2 s in 3T3 fibroblasts[15–17], with new developments

bioRxiv preprint doi: https://doi.org/10.1101/309245; this version posted April 30, 2018. The copyright holder for this preprint (which was not certified by peer review) is the author/funder. All rights reserved. No reuse allowed without permission.

for fully automated analysis (See Methods and Supplementary Figure 2). We combined this assay with the patch-clamp technique in order to dialyse the relevant peptide inside the cellular cytoplasm to inhibit endocytosis acutely. Each recording consisted of 5 min in "cell-attached" mode (CA) with no dialysis followed by 10 min in "whole cell" mode (WC) during which the inhibitors were dialysed (Figure 2A,B). Each recording therefore had its own internal control condition, *i.e.* the cell-attached mode, from which we obtained the frequency ratio f = F_{WC}/F_{CA}, where F is the event frequency recorded during the indicated mode. Of note, the electrical parameters of patch clamp recordings were similar in all conditions (Supplementary Figure 3). We assessed the innocuousness and quantitative nature of this assay by monitoring the endocytic activity of unperturbed cells vs. cells dialysed with either a control solution (see methods for composition) or a solution in which GTP is replaced by its non-hydrolysable form, GTPγS, which prevents the GTP-hydrolysis dependent activity of dynamin[4,5]. Patching the cells minimally affected their endocytic activity over a 10 min period (event frequency f = 67.3 ± 4.3 %, n = 60, vs. 90.7 ± 14.9 % in "no patching" recordings, n = 8, p = 0.58). Oppositely, dialysis of GTPγS rapidly abolished CCV formation (Figure 2C,D) (f = 11.2 ± 4.1 %, n = 4, p < 0.0001). We then compared the inhibitory activities of dynPRD derived peptides. When used at 1 mM, D15, but not an inactive non-sense sequence, partially inhibited endocytosis within 10 min (f = 38.2 ± 3.9 %, n = 22, p = 0.0002, Figure 2B-D), and it hardly had any effect at 100 µM (f = 59.0 ± 5.0 %, n = 13, p = 0.98) (Figure 2D). This is consistent with D15 having a low affinity for its target. On the other hand, using 1 mM of D44 abolished endocytosis almost completely, (f = 20.6 ± 5.2 %, n = 15, p <0.0001). Even 100 µM of either D44 or D30, a trimmed down version of D44 bearing the two SH3 binding motifs (Figure 1A), partially inhibited endocytosis (f = 41.4 ± 9.6 % and 41.7 ± 5.4 %, p = 0.03 and 0.04, respectively). Finally, the divalent peptides dD15-N and dD15-C also had a clearly increased efficiency over D15 (Figure 2B-D), with the C terminal version being the most potent D15-derived inhibitor of endocytosis (f = 13.3 ±3.7 % n = 6, p<0.0001). Overall, the increased efficiency of D44 and divalent D15 peptides in inhibiting endocytosis in living cells is reminiscent of the *in vitro* behaviour described above. Thus, these data suggest that dynamin binding partners may be present in a multimeric configuration in the cellular context.

We tested this hypothesis further by investigating whether the presence of multiple binding sites along dynPRD is also important for the role of dynamin in CME. We based our

bioRxiv preprint doi: https://doi.org/10.1101/309245; this version posted April 30, 2018. The copyright holder for this preprint (which was not certified by peer review) is the author/funder. All rights reserved. No reuse allowed without permission.

approach on rescuing CME in dynamin triple knock-out (TKO) cells[18,19] by re-expressing dynamin2 mutants (Figure 3A). First, we confirmed the knock-out of endogenous dynamins and re-expression of dyn2-GFP to comparable levels by Western blot (Figure 3B, Supplementary Figure 4A). We also validated the ability of dyn2-GFP to rescue CME by monitoring the uptake of Alexa568 labelled transferrin (A568-Tfn). Wild-type dyn2-GFP fully rescued the uptake of A568-Tfn (103.7 ± 7.5 % of control, $p > 0.99$), normally abolished in TKO cells (22.8 ± 1.6 %, $p < 0.0001$, Figure 3C,E). We additionally verified that dyn2-GFP expression levels did not influence A568-Tfn internalisation (Supplementary Figure 4B) such that we could pool the data obtained with a given construct as a single dataset. Then, we tested dyn2-GFP mutated in the C-terminal portion of the PRD as illustrated in Figure 3D. As expected[18], neither re-expression of dyn2-GFP lacking the whole PRD domain (dyn2-GFP-ΔPRD) nor the D15-containing C-terminal domain (dyn2-GFP-ΔCter) could rescue endocytosis in those cells (Figure 3E). We noted that the C-terminal part of dyn2 PRD has three SH3 binding motifs. We labelled them A, B and C (Figure 3D) with motif B being part of the D15 peptide, and motifs A and C flanking motif B. Interestingly, dyn2-GFP mutated at the 6 arginine residues present in these motifs (dyn2-GFP-ABC_{mut}) was also unable to rescue endocytosis (Figure 3E). Oppositely, mutating motif B alone (dyn2-GFP-B_{mut}) resulted in a partial rescue of endocytosis (Figure 3E). This suggests that the flanking binding motifs A and/or C play a role in the rescue process. To further dissect their relevance as potential stabilisation sites for the PRD-SH3 interaction, we mutated them individually. Mutating flanking motif A alone (dyn2-GFP-A_{mut}) permitted a full rescue of CME. On the other hand, mutating flanking motif C alone (dyn2-GFP-C_{mut}) only allowed a partial rescue, to a similar extent as mutating the core B motif alone. These results thus reveal that motif B is not the sole determinant of dynamin function in CME. Hence our working model: binding of amphiphysin to the PRD requires the core B motif as well as a stabilisation site. Under normal conditions, this is achieved by binding to motif C. However, when this site is unavailable, motif B appears to be stabilised enough to impart the partial rescue. The prime candidate for this partial stabilisation is the flanking motif A, which when mutated alone appeared to play no role. We confirmed this hypothesis by mutating motifs A and C simultaneously (dyn2-GFP-AC_{mut}). Under these conditions, the rescue of endocytosis was very poor (albeit significantly above the inactive mutants dyn2-GFP-ΔPRD, ΔCter and ABC_{mut}). Again, this confirms that the B (D15) motif alone is not enough to ensure its functional recruitment. Consistent with these results on Tfn uptake, mutant dyn2-GFP localisation in cells

bioRxiv preprint doi: https://doi.org/10.1101/309245; this version posted April 30, 2018. The copyright holder for this preprint (which was not certified by peer review) is the author/funder. All rights reserved. No reuse allowed without permission.

was very different, from punctate for the active constructs (dyn2-GFP and dyn2-GFP-A_{mut}) to homogenous for the inactive mutants (dyn2-GFP-ΔPRD/ΔCter/ABC_{mut}) and intermediate for the partial mutants (Figure 3F).

To understand at which stage of CME dynamin function was affected, we analysed its recruitment using TIRF imaging in living cells. We compared the kinetics of dyn2-GFP recruitment in TKO cells expressing four different dyn2-GFP constructs, showing various degrees of rescue of CME (WT, ΔCter, B_{mut} and AC_{mut}), with genome-edited SKMEL cells expressing dyn2-GFP in the endogenous gene locus[20] (Figure 4A). As seen for fixed cells, mutated dyn2-GFP constructs had much more homogenous distributions than WT constructs, expressed either in TKO cells or in genome edited cells (Figure 4A). The average cell fluorescence outside clusters was significantly higher in mutants than in WT cells (Figure 4B). In all cases, except for the ΔCter mutant where fluorescence was completely homogenous, transient fluorescent clusters were observed. The frequency of transient clusters was correlated with the ability of the construct to rescue CME: highest for dyn2-GFP-WT re-expression, intermediate for dyn2-GFP-B_{mut} low for dyn2-GFP-AC_{mut} and essentially 0 for dyn2-GFP-ΔCter (Figure 4C). However, the peak amplitude (Figure 4D) and kinetics (Figure 4E) of these recruitment events were similar in all conditions, including genome-edited cells. This suggests that the PRD-SH3 interaction regulates the probability of recruiting dynamin but that once it is initiated it proceeds in a stereotyped manner to complete CCV formation. Next, we directly assessed CCV formation enabled by the dyn2 mutants with the ppH assay. We co-transfected TKO cells with TfR-SEP and dyn2-mCherry constructs (Figure 5). TfR-SEP was clustered in CCSs in cells co-transfected with dyn2-mCherry-WT or dyn2-mCherry-B_{mut}, but was homogenously distributed on the plasma membrane in cells expressing dyn2-mCherry-ΔCter or dyn2-mCherry-AC_{mut} (Figure 5A). This is likely due to the redistribution of TfR to the plasma membrane and saturation of CCSs as already observed in TKO cells [18]. We detected nascent CCVs with the ppH assays in cells co-transfected with dyn2-mCherry and dyn2-mCherry-B_{mut} at frequencies of 0.025 ± 0.009 and 0.004 ± 0.002 $ev.min^{-1}.\mu m^{-2}$, respectively. This significant difference ($p = 0.016$) reflects the changes in Tfn uptake observed (Figure 3E). On the other hand, we observed some moving vesicles at pH 5.5 in cells co-transfected with dyn2-mCherry-ΔCter or dyn2-mCherry-AC_{mut} but the high intracellular background and lack of clustering on the plasma membrane precluded further characterization. We thus moved on to

bioRxiv preprint doi: https://doi.org/10.1101/309245; this version posted April 30, 2018. The copyright holder for this preprint (which was not certified by peer review) is the author/funder. All rights reserved. No reuse allowed without permission.

compare endocytic events in cells transfected with either dyn2-mCherry or dyn2-mCherry-B_{mut}. In both cases, dynamin recruitment was readily observed and peaked at the time of CCV formation (Figure 5C-E) as observed previously[15,17]. Remarkably, the peak fluorescence at the time of scission (-2 s) was smaller for cells expressing dyn2-mCherry-B_{mut} than cells expressing dyn2-mCherry-WT (Figure 5D-F). This could be due to a desynchronization of dynamin recruitment relative of scission. However, the recruitment kinetics of both dynamins relative to CCV formation (Figure 5G), as well as the histograms of peak recruitment of individual events (Figure 5G), were similar before scission, arguing against this possibility. Therefore, we conclude that destabilisation of the dynPRD-SH3 interaction reduces the amount of dynamin at the time of scission.

Taken together, the data presented here support the idea that dynamin-SH3 interactions rely on the presence of multiple interaction sites to achieve successful membrane scission. We showed that D15 alone was a poor binder to its reported target amphSH3 in either mono- (SUMO-amphSH3) or oligomeric (Ntr-bSUMO-amphSH3) forms, whereas both the elongated D44 peptide and the divalent D15 peptides bound with stronger avidity to oligomeric amphSH3. These properties were fully consistent with our *in cellulo* data such that dialysing D44 or divalent D15 peptides inside 3T3 cells inhibited CCV formation fully whereas inhibition by monovalent D15 was only partial. To our knowledge, despite the recognized importance of multivalent interactions for the endocytic process[6], divalent peptides have never been used to interfere with endocytosis in living cells. Considering the moderate inhibitory activity of D15, the D44 and dD15 peptides described here appear to be better tools for this purpose. However, long peptides such as D44 are more difficult to obtain than shorter peptides such as D15 due to the inherent limitations of solid-phase peptide synthesis. In this context, divalent peptides present the advantage of being accessible with significantly less synthetic steps as compared to D44[21] (see methods for details). We therefore propose that the importance of multimeric interactions for dynamic protein assemblies in cells, an emerging field in cell biology[22], can be deciphered using such tools.

We also show that two class-II consensus SH3 interaction motifs have to be present in dynPRD for mutant dynamin to rescue at least in part the endocytic defects observed in dynamin TKO cells and to regulate the kinetics of dynamin recruitment. The central B motif, from which the D15 is derived, is important but not essential; the C-terminal C motif appears

bioRxiv preprint doi: https://doi.org/10.1101/309245; this version posted April 30, 2018. The copyright holder for this preprint (which was not certified by peer review) is the author/funder. All rights reserved. No reuse allowed without permission.

to play a similar role. Interestingly, this second motif is only found in dynamin 2, which could explain its better ability to rescue CME in cell lines than the neuronal dynamin 1[23] and the greater sensitivity of neuronal cells to D15 cytoplasmic dialysis[4]. Similar to motif B (PSRPVRI), motif C also contains an extra arginine after the type II binding motif (PGVPSRR), making it a preferred ligand for amphSH3[11,24]. However, we clearly show with TKO cell rescue experiments that isolated motifs cannot bind stably multivalent ligands. We propose that as long as dynamin and amphiphysin are found in the cytoplasm as homo-dimers[25,26], they cannot strongly interact together and can only form short-lived transient complexes (Figure 5I). However, when amphiphysin is recruited to the neck of vesicles thanks to its curvature sensing properties[26] its SH3 domains may rearrange in such a way that they would be found in close proximity and made available for dynamin binding[27]. Whether amphSH3 domains are optimally placed to face dynPRD in a cellular environment remains unknown. The structure of dynamin has been solved by crystallography[28,29] or cryoEM[30,31] in many different conformations but always without its unstructured PRD. Moreover, dynPRD binding to amphSH3 competes with an intramolecular interaction between the BAR and SH3 domain as was seen for other proteins involved in CME, syndapin 1[32] or endophilin[27]. Therefore, a reciprocal stabilisation of the interaction between dynamin and amphiphysin would occur through this multimeric interaction. The open configuration would only be possible once the neck of the vesicle is tight enough for a scaffold to form around it. This would provide a seed for further recruitment around the vesicle neck for efficient scission. Consistent with this model is the observation that dynamin burst recruitment ~20 s before scission coincides with amphiphysin and endophilin recruitment[15] and that affecting dynamin recruitment kinetics also affects endophilin recruitment kinetics[33]. The coincidence of this precise geometry and the increased avidity conferred by multimerisation as highlighted by this study therefore provide an elegant explanation for the timely presence of dynamin at the moment of membrane scission.

bioRxiv preprint doi: https://doi.org/10.1101/309245; this version posted April 30, 2018. The copyright holder for this preprint (which was not certified by peer review) is the author/funder. All rights reserved. No reuse allowed without permission.

References

1. Ferguson, S. M. & De Camilli, P. Dynamin, a membrane-remodelling GTPase. *Nat. Rev. Mol. Cell Biol.* (2012). doi:10.1038/nrm3266

2. Antonny, B. *et al.* Membrane fission by dynamin: what we know and what we need to know. *EMBO J.* e201694613 (2016). doi:10.15252/embj.201694613

3. Shupliakov, O. Synaptic Vesicle Endocytosis Impaired by Disruption of Dynamin-SH3 Domain Interactions. *Science* **276,** 259–263 (1997).

4. Yamashita, T., Hige, T. & Takahashi, T. Vesicle endocytosis requires dynamin-dependent GTP hydrolysis at a fast CNS synapse. *Science* **307,** 124–127 (2005).

5. Jockusch, W. J., Praefcke, G. J. K., McMahon, H. T. & Lagnado, L. Clathrin-Dependent and Clathrin-Independent Retrieval of Synaptic Vesicles in Retinal Bipolar Cells. *Neuron* **46,** 869–878 (2005).

6. Schmid, E. M. & McMahon, H. T. Integrating molecular and network biology to decode endocytosis. *Nature* **448,** 883–888 (2007).

7. Meinecke, M. *et al.* Cooperative Recruitment of Dynamin and BIN/Amphiphysin/Rvs (BAR) Domain-containing Proteins Leads to GTP-dependent Membrane Scission. *J. Biol. Chem.* **288,** 6651–6661 (2013).

8. Simpson, F. *et al.* SH3-domain-containing proteins function at distinct steps in clathrin-coated vesicle formation. *Nat. Cell Biol.* **1,** 119–124 (1999).

9. Owen, D. J. *et al.* Crystal structure of the amphiphysin-2 SH3 domain and its role in the prevention of dynamin ring formation. *EMBO J.* **17,** 5273–5285 (1998).

10. Takei, K., Slepnev, V. I., Haucke, V. & De Camilli, P. Functional partnership between amphiphysin and dynamin in clathrin-mediated endocytosis. *Nat. Cell Biol.* **1,** 33–39 (1999).

11. Grabs, D. *et al.* The SH3 domain of amphiphysin binds the proline-rich domain of dynamin at a single site that defines a new SH3 binding consensus sequence. *J. Biol. Chem.* **272,** 13419–13425 (1997).

12. Lüscher, C. *et al.* Role of AMPA receptor cycling in synaptic transmission and plasticity. *Neuron* **24,** 649–658 (1999).

13. Solomaha, E., Szeto, F. L., Yousef, M. A. & Palfrey, H. C. Kinetics of Src Homology 3 Domain Association with the Proline-rich Domain of Dynamins: SPECIFICITY, OCCLUSION, AND THE EFFECTS OF PHOSPHORYLATION. *J. Biol. Chem.* **280,** 23147–23156 (2005).

14. Fabrini, R. *et al.* Monomer-dimer equilibrium in glutathione transferases: a critical re-examination. *Biochemistry (Mosc.)* **48,** 10473–10482 (2009).

bioRxiv preprint doi: https://doi.org/10.1101/309245; this version posted April 30, 2018. The copyright holder for this preprint (which was not certified by peer review) is the author/funder. All rights reserved. No reuse allowed without permission.

15. Taylor, M. J., Perrais, D. & Merrifield, C. J. A High Precision Survey of the Molecular Dynamics of Mammalian Clathrin-Mediated Endocytosis. *PLoS Biol.* **9,** e1000604 (2011).

16. Merrifield, C. J., Perrais, D. & Zenisek, D. Coupling between Clathrin-Coated-Pit Invagination, Cortactin Recruitment, and Membrane Scission Observed in Live Cells. *Cell* **121,** 593–606 (2005).

17. Shen, Y., Rosendale, M., Campbell, R. E. & Perrais, D. pHuji, a pH-sensitive red fluorescent protein for imaging of exo- and endocytosis. *J. Cell Biol.* **207,** 419–432 (2014).

18. Ferguson, S. *et al.* Coordinated Actions of Actin and BAR Proteins Upstream of Dynamin at Endocytic Clathrin-Coated Pits. *Dev. Cell* **17,** 811–822 (2009).

19. Park, R. J. *et al.* Dynamin triple knockout cells reveal off target effects of commonly used dynamin inhibitors. *J. Cell Sci.* **126,** 5305–5312 (2013).

20. Doyon, J. B. *et al.* Rapid and efficient clathrin-mediated endocytosis revealed in genome-edited mammalian cells. *Nat. Cell Biol.* **13,** 331–337 (2011).

21. Sainlos, M. *et al.* Biomimetic divalent ligands for the acute disruption of synaptic AMPAR stabilization. *Nat. Chem. Biol.* **7,** 81–91 (2011).

22. Banani, S. F., Lee, H. O., Hyman, A. A. & Rosen, M. K. Biomolecular condensates: organizers of cellular biochemistry. *Nat. Rev. Mol. Cell Biol.* **18,** 285–298 (2017).

23. Liu, Y.-W. *et al.* Differential curvature sensing and generating activities of dynamin isoforms provide opportunities for tissue-specific regulation. *Proc. Natl. Acad. Sci.* **108,** E234–E242 (2011).

24. Landgraf, C. *et al.* Protein Interaction Networks by Proteome Peptide Scanning. *PLoS Biol.* **2,** e14 (2004).

25. Faelber, K. *et al.* Structural Insights into Dynamin-Mediated Membrane Fission. *Structure* **20,** 1621–1628 (2012).

26. Peter, B. J. BAR Domains as Sensors of Membrane Curvature: The Amphiphysin BAR Structure. *Science* **303,** 495–499 (2004).

27. Mim, C. *et al.* Structural basis of membrane bending by the N-BAR protein endophilin. *Cell* **149,** 137–145 (2012).

28. Faelber, K. *et al.* Crystal structure of nucleotide-free dynamin. *Nature* **477,** 556–560 (2011).

29. Reubold, T. F. *et al.* Crystal structure of the dynamin tetramer. *Nature* **525,** 404–408 (2015).

30. Chappie, J. S. *et al.* A pseudoatomic model of the dynamin polymer identifies a hydrolysis-dependent powerstroke. *Cell* **147,** 209–222 (2011).

bioRxiv preprint doi: https://doi.org/10.1101/309245; this version posted April 30, 2018. The copyright holder for this preprint (which was not certified by peer review) is the author/funder. All rights reserved. No reuse allowed without permission.

31. Sundborger, A. C. *et al.* A dynamin mutant defines a superconstricted prefission state. *Cell Rep.* **8,** 734–742 (2014).

32. Rao, Y. *et al.* Molecular basis for SH3 domain regulation of F-BAR-mediated membrane deformation. *Proc. Natl. Acad. Sci. U. S. A.* **107,** 8213–8218 (2010).

33. Taylor, M. J., Lampe, M. & Merrifield, C. J. A Feedback Loop between Dynamin and Actin Recruitment during Clathrin-Mediated Endocytosis. *PLoS Biol.* **10,** e1001302 (2012).

34. Grillo-Bosch, D., Rabanal, F. & Giralt, E. Improved Fmoc-based solid-phase synthesis of homologous peptide fragments of human and mouse prion proteins. *J. Pept. Sci. Off. Publ. Eur. Pept. Soc.* **17,** 32–38 (2011).

35. Käll, L., Canterbury, J. D., Weston, J., Noble, W. S. & MacCoss, M. J. Semi-supervised learning for peptide identification from shotgun proteomics datasets. *Nat. Methods* **4,** 923–925 (2007).

36. Cao, H., Garcia, F. & McNiven, M. A. Differential distribution of dynamin isoforms in mammalian cells. *Mol. Biol. Cell* **9,** 2595–2609 (1998).

bioRxiv preprint doi: https://doi.org/10.1101/309245; this version posted April 30, 2018. The copyright holder for this preprint (which was not certified by peer review) is the author/funder. All rights reserved. No reuse allowed without permission.

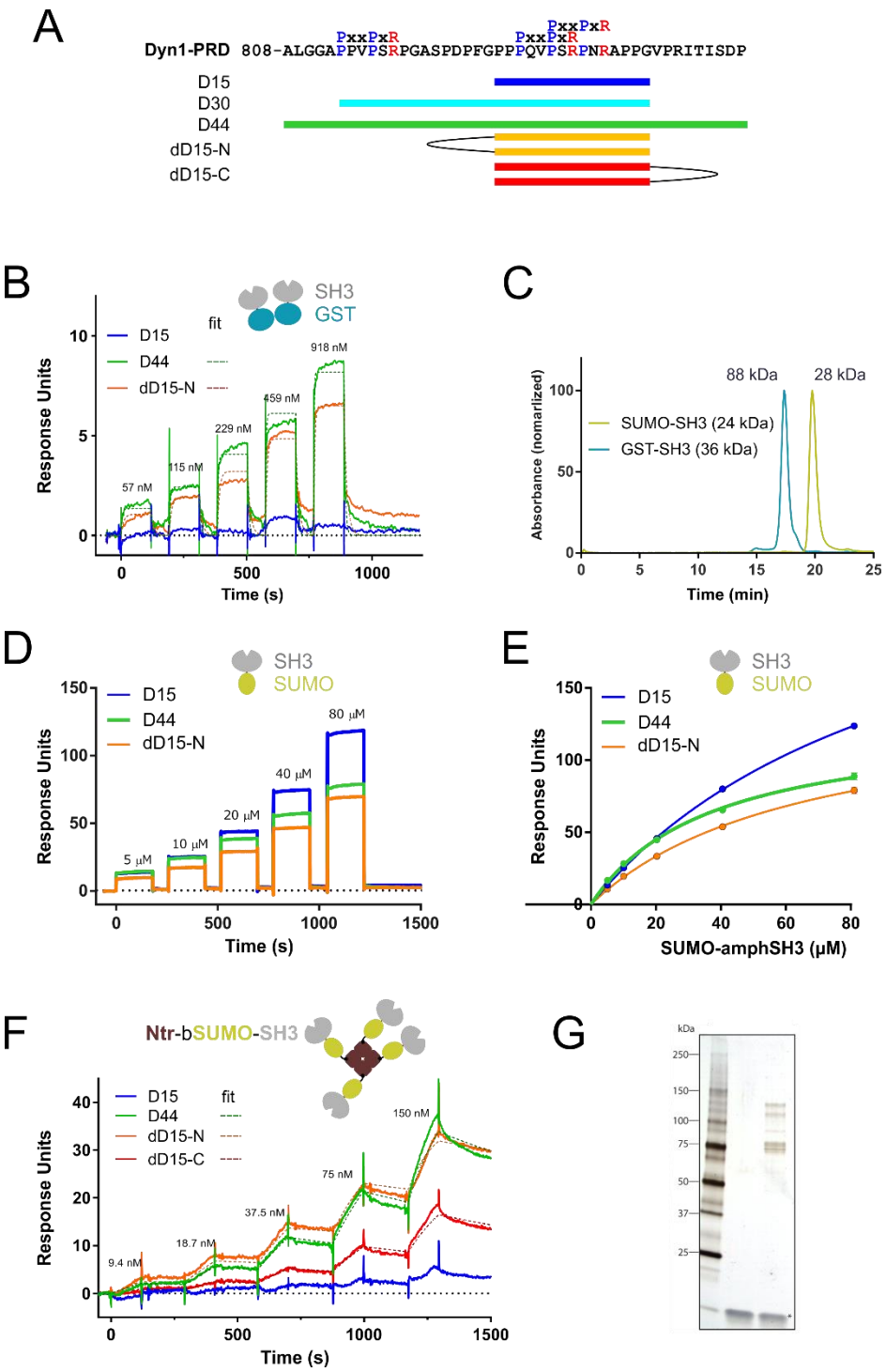

Figure 1: Multimeric SH3 domains bind with high affinity to D44 and divalent but not monovalent D15 peptides. A, Scheme of the peptides used in this study. Top, sequences of the last 44 residues of rat dynamin1 (splice variant b). **B**, Representative sensorgrams of GST-SH3 binding at indicated concentrations to immobilized peptides. The scheme on top (GST in blue, SH3 in gray) indicates that this protein likely forms dimers (see F). **C**, Retention times of SUMO-SH3 and GST-SH3 measured by size exclusion chromatography. The theoretical molecular weights are indicated. For SUMO-SH3 the elution peak corresponds to 28 kDa, close to the expected monomer, whereas for GST-SH3 it corresponds to 88 kDa, close to the expected size of a dimer. **D**, Representative sensorgrams of SUMO-SH3 binding at indicated

bioRxiv preprint doi: https://doi.org/10.1101/309245; this version posted April 30, 2018. The copyright holder for this preprint (which was not certified by peer review) is the author/funder. All rights reserved. No reuse allowed without permission.

concentrations to immobilized peptides. Note the fast on and off rates for all peptides consistent with weak and transient interactions. **E**, Steady-state K_Ds calculated from the data in D (3 replicate experiments): 102 ± 2 µM (D15), 37 ± 2 µM (D44), 66 ± 3 µM (N-P3D15). **F**, Representative sensorgrams of Ntr-bSUMO-SH3 binding at indicated concentrations to immobilized peptides. The scheme on top shows the multimeric complex formed by bSUMO-SH3 bound to tetrameric neutravidin (brown). Note the change in kinetics (slower off rates) for D44 and the multimeric peptides (dD15-N and dD15-C). **G**, Silver stain of rat brain lysate pull-down with no peptide (middle) or biotinylated dD15-N (right).

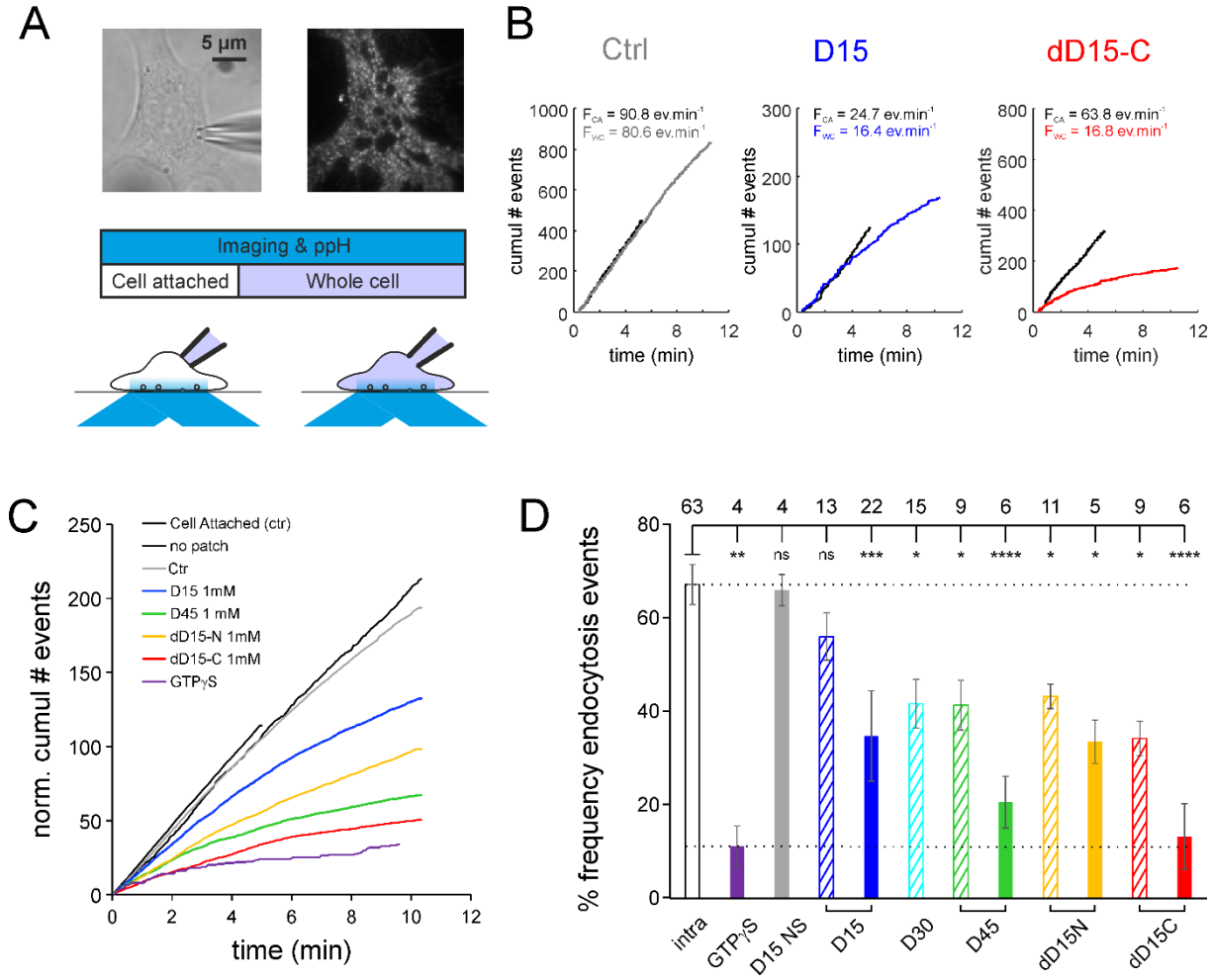

Figure 2: D44 and divalent D15 peptides are more efficient than D15 to block CME monitored with the ppH assay. A, Experimental design. Top, images of a 3T3 cell recorded with a patch-clamp electrode (seen on the transmitted light image, *left*) and transfected with TfR-SEP imaged with TIRF microscopy (*right*). The cells are recorded for at least 15 min with the ppH assay. In the first 5 min, the cell is in the cell attached configuration (*left*) and in the last 10 min in the whole cell configuration (*right*). **B**, Examples of recordings of cells with internal solutions containing no peptide (Ctrl, left), 1 mM D15 (middle) or 1 mM dD15-C (right). Black lines represent the cumulative number of detected endocytosis events over time in cell attached configuration. They are all straight lines, indicating that the event frequency remains

bioRxiv preprint doi: https://doi.org/10.1101/309245; this version posted April 30, 2018. The copyright holder for this preprint (which was not certified by peer review) is the author/funder. All rights reserved. No reuse allowed without permission.

constant during recording. This frequency F_{CA} is written on top of the graph. Lines in color represent the cumulative number of events in whole cell configuration. Note that at early time points these curves are tangential to the corresponding curves in cell attached, indicating the same endocytosis activity. In the example with the control solution, the slope of this curve remains constant with only a slight deflection towards the end of the recording. On the other hand, the deflections are much more marked with solution containing inhibitory peptides. The frequency F_{WC} in the last two minutes of the whole cell recording is indicated on top of the graphs. **C**, Averages of curves normalized to the corresponding cell attached recordings and displayed as in B for all the conditions tested in this study. **D**, Average ± SEM of the ratio of event frequency measured 8-10 min in whole cell over event frequency 3-5 min in cell attached for the same cell. The number of recordings for each condition is indicated on top of the graph. Recording solutions containing 100 µM (*hatched bars*) or 1 mM (*plain bars*) of the indicated peptide.

bioRxiv preprint doi: https://doi.org/10.1101/309245; this version posted April 30, 2018. The copyright holder for this preprint (which was not certified by peer review) is the author/funder. All rights reserved. No reuse allowed without permission.

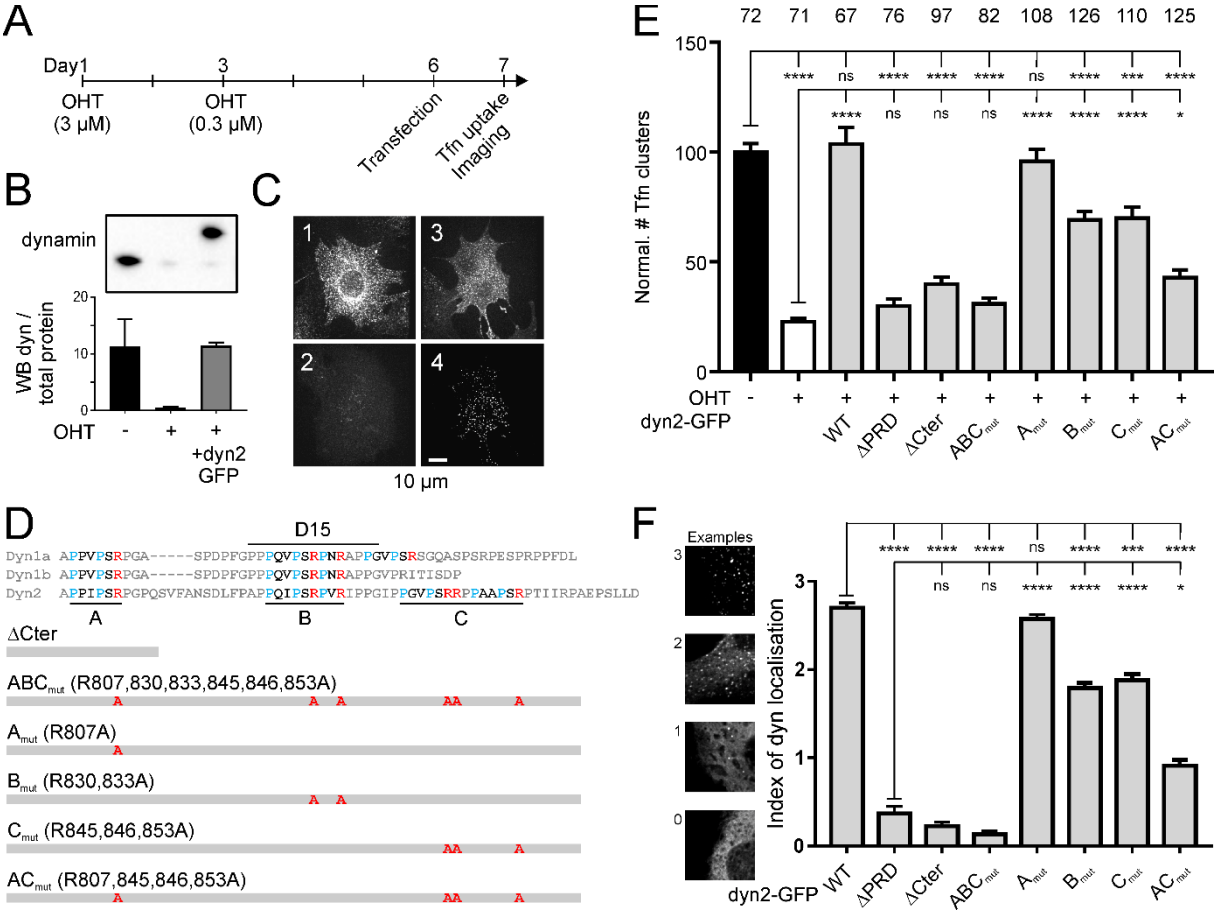

Figure 3: Rescue of endocytosis in dynamin TKO cells with PRD mutant dynamins. A, Protocol for dynamin knock-out and rescue. After 6 days of gene excision of the three dynamin genes following hydroxytamoxifen (OHT) treatment, cells are transfected with electroporation. Tfn uptake and imaging assays are performed the next day. **B**, Western blot with pan-dynamin antibody on untreated cells, cells treated with OHT or cells treated and transfected with dynamin2-GFP. Note the migration at higher molecular weight of dyn2-GFP. Bottom, quantification in three experiments of the WB signal normalized to the total amount of protein. See Supplementary Figure 4A for full gels and blots. **C**, Example images of cells not treated with OHT (1), treated with OHT (2), treated and transfected with dyn2-GFP (3) incubated with Tfn-A458 for five minutes, washed and fixed. (4) Image of dyn2-GFP of the cell shown in (3). **D**, Sequences of the C terminal parts of the PRD of dyn1 (a and b splice variants) and dyn2, with the class-II SH3 binding motifs A, B and C indicated. Below, mutants of dyn2 used to rescue Tfn-A568 uptake with the corresponding mutations. **E**, Quantification of Tfn-A568 uptake, expressed as the density of detected clusters for cells treated with OHT as indicated and transfected with dyn2-GFP mutants. The number of cells imaged in four different experiments is indicated on top of each condition. The adjusted p values of 1-way ANOVA followed by Tukey's multiple comparison tests are shown in Supplementary Table 2. **F**, Quantification of dyn2-GFP localization in transfected TKO cells. Each cell was evaluated blind with a score ranging from 0 (homogenous labelling) to 3 (punctuate labelling without homogenous), with intermediates of 1 (mostly homogenous with few clusters) and 2 (some homogenous with distinct clusters). Examples in the left illustrate this scoring. The graphs show the average ± SEM of scores for each dyn2 mutant.

bioRxiv preprint doi: https://doi.org/10.1101/309245; this version posted April 30, 2018. The copyright holder for this preprint (which was not certified by peer review) is the author/funder. All rights reserved. No reuse allowed without permission.

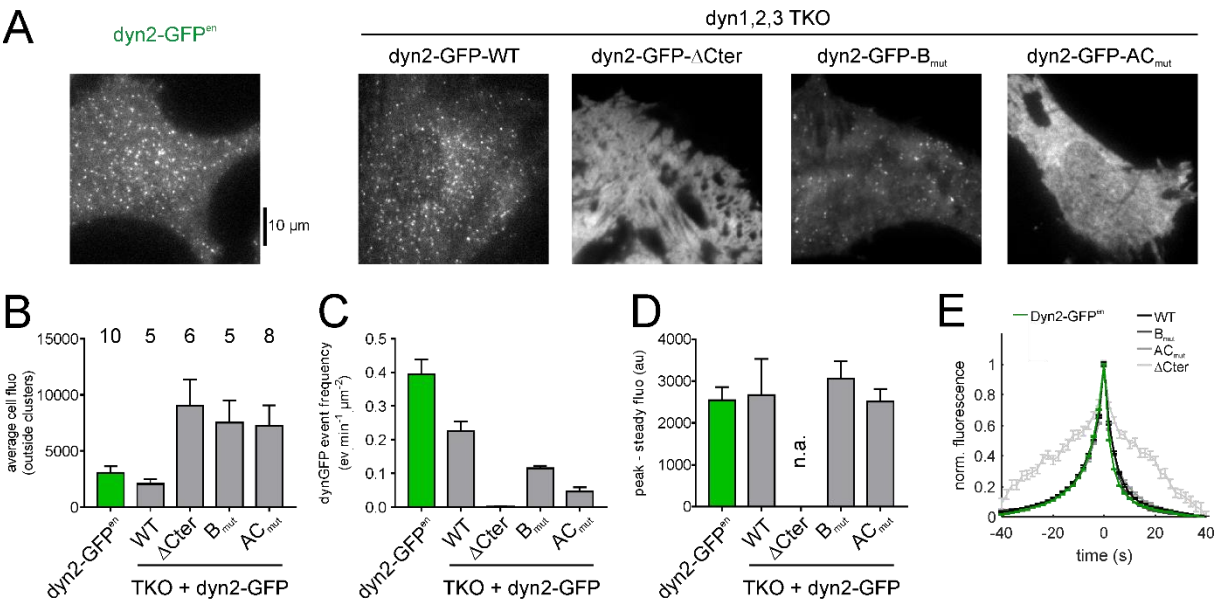

Figure 4: The frequency of dyn2-GFP recruitment events is affected in dynPRD mutants. A, TIRF images of living SKMEL cells expressing dyn2-GFP in both endogenous loci (left) or dynamin TKO MEF cells transfected with the indicated dyn2-GFP constructs (right). **B**, Average fluorescence outside the dyn2-GFP clusters for the various dyn2-GFP mutants. The number of cells recorded is indicated at the top of the graph. **C**, dyn2-GFP recruitment event frequencies for the same cells as in B. **D**, Average amplitudes of peak dyn2-GFP events for the same cells as in B, except for cells transfected with dyn2-GFP-ΔCter. **E**, Normalized average fluorescence of all the events detected, aligned to their peak fluorescence. The total number of events averaged was 36070 for dyn2-GFPen cells and 18678, 127, 5916 and 6116 for TKO cells transfected with dyn2-GFP-WT, dyn2-GFP-ΔCter, dyn2-GFP-B_{mut} and dyn2-GFP-AC_{mut}, respectively. Note that the curves largely overlap except for the 127 events detected in cells expressing dyn2-GFP-ΔCter, reflecting the background of the detection and alignment procedure.

bioRxiv preprint doi: https://doi.org/10.1101/309245; this version posted April 30, 2018. The copyright holder for this preprint (which was not certified by peer review) is the author/funder. All rights reserved. No reuse allowed without permission.

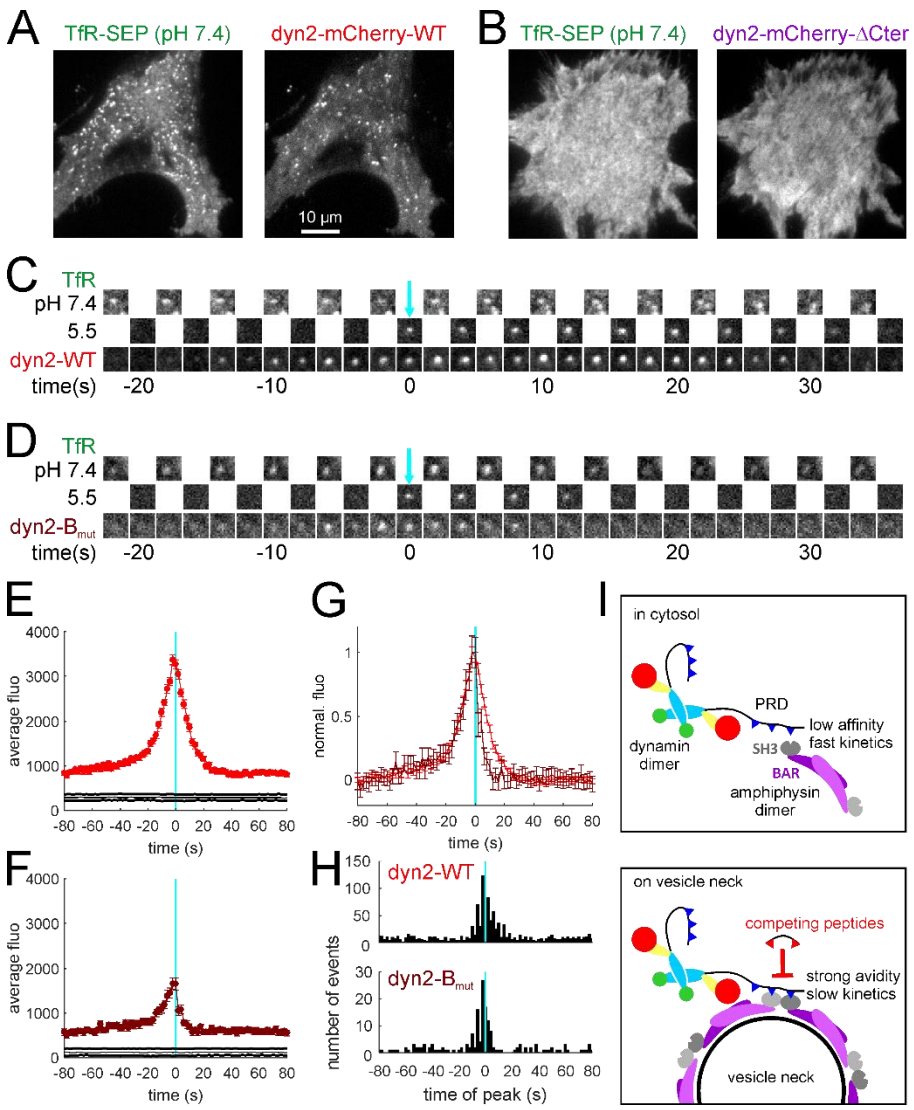

Figure 5: Recruitment kinetics of dyn2 PRD mutants to forming endocytic vesicles. A, Images of TKO cells co-transfected with TfR-SEP and dyn2-mCherry-WT (left) or dyn2-mCherry-ΔCter (right). Not the punctuated pattern of both markers with dyn2-WT which becomes homogenous with dyn2ΔCter. **C**, Example of a scission event recorded in the cell shown in A (left). Note the transient recruitment of dyn2-mCherry-WT which peaks around time 0. **D**, Same as C for a TKO cell co-transfected with TfR-SEP and dyn2-mCherry-B_{mut}. **E**, Average fluorescence of dyn2-mCherry of 1193 events recorded in 5 cells co-transfected with TfR-SEP and dyn2-mCherry-WT and aligned to the time of scission (cyan line). The black lines indicate 95% confidence intervals for significant recruitment. **F**, Same as E for 171 events recorded in 7 cells co-transfected with TfR-SEP and dyn2-mCherry-B_{mut}. **G**, The curves in E,F are normalized to their peak. **H**, Histograms of peak dyn2 recruitment in single events. **I**, Model of dynamin recruitment by its PRD domain with SH3 containing proteins. In solution, dynamin forms a dimer, as well as SH3 domain containing proteins such as amphiphysin. The SH3 domains of the dimer are too far apart to stabilize the interaction with the PRD via multiple binding motifs. On the vesicle neck, two dimers of amphiphysin are arranged such that two SH3 domains are next to each other.

bioRxiv preprint doi: https://doi.org/10.1101/309245; this version posted April 30, 2018. The copyright holder for this preprint (which was not certified by peer review) is the author/funder. All rights reserved. No reuse allowed without permission.

Methods

Peptide synthesis

Abbreviations: DCM: Dichloromethane; DHB: 2,5-Dihydroxybenzoic acid; DIPEA:N,N'-diisopropylethylamine DMF: N,N-dimethylformamide; Fmoc: 9-fluorenylmethoxy-carbonyl; Fmoc-TTDS: [N1-(Fmoc)-1,13-diamino-4,7,10-trioxatridecan-succinamic acid; HBTU: 2-(1H-Benzotriazol-1-yl)-1,1,3,3-tetramethyluronoium hexafluorphosphate; HOBt: 1-hydroxy-benzotriazole; MALDI: Matrix-assisted laser desorption ionisation; MeCN: Acetonitrile; MS: Mass spectrometry; NMP: N-methyl-2-pyrrolidone; RP-HPLC: Reverse-phase high performance liquid chromatography; Pbf: pentamethyl-2,3-dihydrobenzofuran-5-sulfonyl; SPPS: Solid-phase peptide synthesis; TIPS: Triisopropylsilane; TFA: Trifluoroacetic acid

Chemicals: Fmoc-protected amino-acids were from GenScript USA Inc. HBTU, Fmoc-TTDS and Fmoc-Lys(N_3)-OH were from Iris Biotech GmbH. HOBt, DIPEA, N-methylpiperidine, acetic anhydride, pyridine, biotin, 4-pentynoic acid, TIPS, TRIZMA base and DHB were from Sigma-Aldrich. TFA, MeCN, DCM, DMF and diethyl Ether were from Fisher scientific. Fmoc-Dab(Alloc)-OH was from Bachem AG. NMP was from Applied Biosystems.

Procedure: Monomeric peptides were synthesised at 0.05 mmol scale on Fmoc-NOVA PEG rink amide AM LL resin (Novabiochem) and dimeric peptides on PAL NovaSyn TG resin (Novabiochem). Amino-acids were assembled by automated SPPS on a CEM micro-waves Liberty-1 synthesiser (Saclay, France) except for C-terminally linked dimeric peptides. Coupling of PEG motifs and N-terminal derivatisations were also performed manually. For automated synthesis, Fmoc protecting groups were cleaved with 4-methylpiperidine in DMF (1:5 v/v) containing 0.1M HOBt using a combination of short (35 W, 75°C, 30s) and a long cycle (35 W, 70°C, 180s). Couplings of Fmoc-protected amino acids (0.2 M) were carried out in the presence of HBTU (0.25 M) and DIPEA (1M) using standard coupling cycles (20 W, 70°C, 300s, except for Fmoc-Arg(Pbf)-OH (0 W, RT, 1500s followed by 20 W, 70°C, 300s). For the synthesis of D44, we evaluated a priori difficult couplings according to [34]. We thus introduced a systematic double coupling on Y1, A2, L3, G5 (N-terminus amino acids) V37, P38, I40 and T41 (bulky amino acids). Other double couplings were then introduced empirically at positions P7, S11, S16, P22, P23, 33, P34, G36, D43 and P44. An acetylation step was systematically introduced after each amino-acid coupling in order to eliminate truncation products. For manual synthesis, Fmoc

bioRxiv preprint doi: https://doi.org/10.1101/309245; this version posted April 30, 2018. The copyright holder for this preprint (which was not certified by peer review) is the author/funder. All rights reserved. No reuse allowed without permission.

protecting groups were cleaved with 4-methylpiperidine in DMF (1:5 v/v, 1x1 min + 2x7 min) except for the final coupling of PEG motifs on N-terminally linked dimeric peptides for which the deprotection was performed using 4-methylpiperidine in NMP (1:5 v/v, 1x1 min + 4x5 min). Couplings of Fmoc-protected amino acid were carried out in the presence of HBTU/HOBt and DIPEA (5:5:10 eq, 1h30min). C-terminally linked dimeric peptides were obtained by generating two points of chain elongation with a Fmoc-Lys(Fmoc)-OH amino acid, whereas N-terminally linked dimeric peptides were obtained by coupling a 7:3 mixture of Fmoc-Lys(N3)-OH and pentynoic acid followed by copper(I)-catalyzed azide-alkyne cycloaddition in DMF/4-methylpiperidine (8:2) with CuI (5 eq), ascorbic acid (10 eq) and aminoguanidine (10 eq). N-free peptide resins were derivatised with acetyl groups or biotin. Acetylation was performed using 7 mL of a solution of 0.15M acetic anhydride and 0.15M pyridine in DMF (1h30min). Biotinylation was performed by first coupling Fmoc-TTDS-OH (3 eq) then biotin (3 eq). Both couplings were mediated by HBTU/ HOBt and DIPEA (3:3:6 eq, 1h30min). Acetylated peptides were used in living cells and for SPR experiments. Biotinylated peptides were used for affinity isolation from rat brain lysates and SPR experiments. . Peptides were cleaved from the resin for 3h using TFA/H_2O/TIPS (95:2.5:2.5) with mild orbital shaking and precipitated with cold diethyl ether. All crude peptides were resuspended in H_2O containing a few drops of DMF and purified in a Waters 1525 semi-preparative RP-HPLC system equipped with a UV/Vis detector and a YMC C18, ODS-A /120, 250 × 20 mm. Purification was performed using a standard gradient of 5% MeCN containing 0.1% TFA for 5 min followed by an appropriate gradient of MeCN containing 0.1% TFA in H_2O for 40 min (1 $mL.min^{-1}$). UV detection was performed at 220 and 280 nm. All peptides were obtained at more than 90% purity as judged by analytical RP-HPLC with the exception of N-P_3-D15 (84.8 % purity). Masses were determined by MALDI-TOF spectroscopy in an UltraFlex III TOF-TOF (Bruker Daltonics). Peptide concentrations were determined by absorbance measurements at 280 nm in a UV-visible spectrophotometer (UV-1800, Shimadzu) ($\varepsilon(Y)$ = 1490 $M^{-1}.cm^{-1}$). Peptides were lyophilised and stored at -80°C until use.

Affinity isolation assays

Frozen adult Sprague-Dawley rat brains (2 x ~1.5g) were thawed in 20 mL ice cold modified RIPA buffer (50 mM Tris pH 7.5, 150 mM NaCl, 0.1% SDS, 0.5% sodium deoxycholate, 1% NP-40, 1 mM EDTA) containing a protease inhibitor mixture (1:1,000; Protease Inhibitor Cocktail

bioRxiv preprint doi: https://doi.org/10.1101/309245; this version posted April 30, 2018. The copyright holder for this preprint (which was not certified by peer review) is the author/funder. All rights reserved. No reuse allowed without permission.

set III; Calbiochem) for about 5 min and cut into small pieces. The tissues were homogenised using a glass/teflon homogeniser. Homogenates were centrifuged at 7,500 g for 25 min at 4 °C to remove cell debris. The supernatant was aliquoted and stored at -80 °C until the affinity-based isolation (pull-down) experiments were performed. Streptavidin-coated beads (Dynabeads M-280, Life Technologies) were washed three times and incubated for 15 min at room temperature (RT) in modified RIPA buffer supplemented with 0.1 % BSA. Rat brain lysates were incubated with the biotinylated peptide (or biotin as a negative control) for 10 min at RT before addition of the beads and further incubation for 5 min at RT. Beads were washed 5 times in RIPA buffer and transferred into new eppendorf tubes. For elution, acetylated ligands were added in excess to the bead suspension and incubated for 5 min at RT. The supernatant was kept for proteomics analysis and electrophoresis followed by silver staining after addition of fresh 6x sample buffer (ProteoSilver Silver Stain Kit, Sigma-Aldrich).

Proteomics analysis

Samples were solubilized in Laemlli buffer and were deposited in triplicate onto SDS-PAGE. Separation was stopped once proteins have entered resolving gel. After colloidal blue staining, bands were cut out from the SDS-PAGE gel and subsequently cut in 1 mm x 1 mm gel pieces. Gel pieces were destained in 25 mM ammonium bicarbonate 50% ACN, rinsed twice in ultrapure water and shrunk in ACN for 10 min. After ACN removal, gel pieces were dried at room temperature, covered with the trypsin solution (10 ng/µl in 50 mM NH_4HCO_3), rehydrated at 4 °C for 10 min, and finally incubated overnight at 37 °C. Spots were then incubated for 15 min in 50 mM NH_4HCO_3 at room temperature with rotary shaking. The supernatant was collected, and an H_2O/ACN/HCOOH (47.5:47.5:5) extraction solution was added onto gel slices for 15 min. The extraction step was repeated twice. Supernatants were pooled and dried in a vacuum centrifuge to a final volume of 25 µL. Digests were finally resuspended in 25 µl of formic acid (5%, v/v) and stored at -20 °C.

Peptide mixture was analyzed on a Ultimate 3000 nanoLC system (Dionex, Amsterdam, The Netherlands) coupled to a nanospray LTQ-Orbitrap XL mass spectrometer (ThermoFinnigan, San Jose, CA). Ten microliters of peptide digests were loaded onto a 300-µm-inner diameter x 5-mm C_{18} PepMap^{TM} trap column (LC Packings) at a flow rate of 30 µL/min. The peptides were eluted from the trap column onto an analytical 75-mm id x 15-cm C18 Pep-Map column (LC

bioRxiv preprint doi: https://doi.org/10.1101/309245; this version posted April 30, 2018. The copyright holder for this preprint (which was not certified by peer review) is the author/funder. All rights reserved. No reuse allowed without permission.

Packings) with a 4–40% linear gradient of solvent B in 35 min (solvent A was 0.1% formic acid in 5% ACN, and solvent B was 0.1% formic acid in 80% ACN). The separation flow rate was set at 300 nL/min. The mass spectrometer operated in positive ion mode at a 2-kV needle voltage. Data were acquired in a data-dependent mode. MS scans (*m/z* 300-1700) were recorded at a resolution of R = 70 000 (@ m/z 400) and an AGC target of 5 x 10^5 ions collected within 500 ms. Dynamic exclusion was et to 30 s and top 6 ions were selected from fragmentation in CID mode. MS/MS scans with a target value of 1 x 10^4 ions were collected in the ion trap with a maximum fill time of 200 ms. Additionally, only +2 and +3 charged ions were selected for fragmentation. Others settings were as follows: no sheath nor auxiliary gas flow, heated capillary temperature, 200 °C; normalized CID collision energy of 35% and an isolation width of 3 m/z.

Data were searched by SEQUEST through Proteome Discoverer 1.4 (Thermo Fisher Scientific Inc.) against a subset of the 2018.01 version of UniProt database restricted to *Rattus norvegicus* Reference Proteome Set (29,961 entries). Spectra from peptides higher than 5000 Da or lower than 350 Da were rejected. The search parameters were as follows: mass accuracy of the monoisotopic peptide precursor and peptide fragments was set to 10 ppm and 0.6 Da respectively. Only b- and y-ions were considered for mass calculation. Oxidation of methionines (+16 Da) and carbamidomethylation of cysteines (+57 Da) were considered respectively as variable and fixed modifications. Two missed trypsin cleavages were allowed. Peptide validation was performed using Percolator algorithm[35] and only “high confidence” peptides were retained corresponding to a 1% False Positive Rate at peptide level.

Raw LC-MS/MS data were imported in Progenesis QI for Proteomics 2.0 (Nonlinear Dynamics Ltd, Newcastle, U.K). Data processing includes the following steps: (i) Features detection, (ii) Features alignment across the 6 samples, (iii) Volume integration for 2-6 charge-state ions, (iv) Normalization on feature median ratio, (v) Import of sequence information, (vi) Calculation of protein abundance (sum of the volume of corresponding peptides), (vii) A statistical test was performed and proteins were filtered based on p-value<0.05. Noticeably, only non-conflicting features and unique peptides were considered for calculation at protein level. Quantitative data were considered for proteins quantified by a minimum of 2 peptides.

bioRxiv preprint doi: https://doi.org/10.1101/309245; this version posted April 30, 2018. The copyright holder for this preprint (which was not certified by peer review) is the author/funder. All rights reserved. No reuse allowed without permission.

SH3 domain production

SUMO-Amph1-SH3 and GST-Amph1-SH3 were generated by subcloning murine Ampiphysin1 SH3 domain residues 607-686) from pAmph1-mCherry (kind gift from C. Merrifield, Addgene 27692) using BamHI and XhoI restriction sites into a modified pET-SUMO bacterial expression vector (Life Technologies) incorporating a TEV cleavage site and a multiple cloning site following the SUMO tag or a modified pGEX-4T-2 vector incorporating a TEV cleavage site before the gene of interest. The biotinylated SUMO-Amph1-SH3 was obtained by subcloning the gene from SUMO-Amph1-SH3 using BsrGI and XhoI restriction sites into a homemade vector derived from pET-24a that presents a biotin acceptor peptide (Avitag) and a His10 tag prior to the gene of interest. The recombinant SH3 domains (SUMO and GST fusions) were produced in BL21-CodonPlus (DE3)-RIPL E. coli cells by auto-induction at 16 °C and purified by affinity (Ni-NTA resin) and size exclusion chromatography as previously described[21]. The biotinylated SUMO-Amph1-SH3 fusion was produced in BL21-CodonPlus (DE3) E. coli cells in presence of a plasmid encoding for BirA in a pACYC-Duet-1 vector and biotin (50 µM) by auto-induction at 16 °C and purified as above. Proteins were stored at -80 °C in surface plasmon resonance running buffer until use. Analytical size exclusion chromatography were performed on a HiLoad Superdex200 Increase 10/300 GL column with PBS + 0.01% Tween-20 as an eluent at a flow rate of 0.75 $mL.min^{-1}$.

Surface plasmon resonance measures and analysis

Experiments were performed at 25 °C with a Biacore™ X100 or T200 apparatus (Biacore™, GE healthcare Life Sciences, Uppsala, Sweden). The experiments were performed on biotin CAPture kit sensor chips (Biacore™). 50-90 RU of biotinylated peptides were immobilised by injecting solutions prepared at 5-10 nM in running buffer (10 mM sodium phosphate buffer, pH 7.4, 150 mM sodium chloride and 0.01% Tween-20). Importantly, for all experiments, density of the monovalent D15 peptide (bound RU) was about two-fold superior to the ones of divalent or D44 peptides to rule out artefact due to high surface density of the ligand. One flow-cell was left blank and used as a reference. For single cycle kinetics experiments, captured targets and analyte samples were prepared in running buffer and injected at 5 and 30 $µl.min^{-1}$ respectively. The capture of streptavidin and regeneration of the functionalised surface was

bioRxiv preprint doi: https://doi.org/10.1101/309245; this version posted April 30, 2018. The copyright holder for this preprint (which was not certified by peer review) is the author/funder. All rights reserved. No reuse allowed without permission.

achieved following the manufacturer's recommended protocols. Sensorgrams were double-referenced using Biacore evaluation software (Biacore). No points were removed prior to data fitting. Spikes still present after the double-referencing process had no influence on the analysis. The kinetic data were analysed using a 1:1 Langmuir binding model of the BIAevaluation software with the bulk refraction index (RI) kept constant and equal to 0 and the mass transfer constant (tc) kept constant and equal to 10^8. In the case of fast association and dissociation rate constants that prevented reliable kinetics analysis, the curves were thus exploited using equilibrium analysis to obtain the dissociation equilibrium constants in GraphPad Prism (GraphPad Software v7.02 for Windows) by fitting the data with the one-site binding hyperbola formula

$$Y = \frac{B_{max} * X}{K_D + X}$$

where Y is the response (in RU), B_{max} is the response value at maximal binding, K_D is the affinity constant to be determined and X is the protein concentration.

Dynamin2 mutant design

Dynamin 2 (human dynamin2bb according to the nomenclature of [36]) plasmids were based on the Dyn2-mCherry construct from Taylor et al. 2011 (Addgene 27689). We generated dyn2-GFP and dyn2-mCherry constructs used in this study in which the GFP/mCherry tag is relocated before the PRD (residue 740) with linkers composed of six residues (GTSGSS). We first generated an unlabeled dyn2 construct by PCR in which we introduced a stop codon at the end of the dynamin ORF. We then generated by PCR a Linker+ GFP/mCherry which we inserted into the dyn2 vector with the In-Fusion HD kit (Clontech). Dyn2-GFP-ΔCter and Dyn2-GFP-ΔPRD were generated introducing a stop codon at positions 807 (after motif A) or 740 (before the PRD), respectively. Single mutation GFP constructs (Dyn2-GFP A_{mut}, B_{mut} and C_{mut}) were generated by directed mutagenesis. Double mutation Dyn2-GFP AC_{mut} was generated sequentially by directed mutagenesis. The Dyn ABC_{mut} was generated by inserting the artificially synthesized PRD (Eurogentec) containing these mutations into the wildtype construct by In-Fusion. All constructs were verified by sequencing.

bioRxiv preprint doi: https://doi.org/10.1101/309245; this version posted April 30, 2018. The copyright holder for this preprint (which was not certified by peer review) is the author/funder. All rights reserved. No reuse allowed without permission.

Cell culture and transfection

NIH 3T3 cells (ECACC 93061524) were cultured in DMEM supplemented with 1% sodium pyruvate, 1% glutamax and 10% fetal calf serum (Invitrogen). Cells were incubated at 37 °C in 5% CO2 unti use and subcultured every 2 to 4 days for maintenance up to passage 20. Cells were transfected with 1.5 µg of TfR-SEP plasmid 24 hours prior to imaging and patch clamp. Care was taken to find the right balance between sufficient fluorescent signal to allow for proper imaging and reasonable overexpression to diminish potential saturation artefacts. Best results were obtained using Fugene 6 (Promega) as the transfection reagent but Lipofectamine 2000 (Invitrogen) has also been used in this study due to a temporary arrest of Fugene 6 production by the provider. All transfections were performed according to the manufacturers' recommendations. 4-8 hours after transfection, cells were seeded at a density of ~70,000 cells.ml^{-1} on 18 mm glass coverslips coated with poly-L-lysine (3 min application of 0.1 mM polylysine (Sigma P2636) in borate buffer, pH 8.0 followed by a quick rinse in PBS) and used the next day.

The mouse embryonic fibroblast cell line obtained from tamoxifen inducible triple dynamin conditional mice (dynamin TKO cells [13]) was a kind gift from Pietro De Camilli (Yale School of Medicine, New Haven, CT). Cells were cultured in DMEM/F12 supplemented with 1% sodium pyruvate, 1% glutamax and 10% fetal calf serum (Invitrogen). Dynamin TKO was induced by the application of 3 µM Hydroxytamoxifen (OHT, Sigma) for 2 days, then 0.3 µM for 4 more days before transfection. Cells were transfected by nucleofection with the kit MEF 1 and the program MEF T20 (Lonza, Switzerland) by mixing 3 µg of DNA (dynamin construct and TfR-SEP if applicable) with 10^6 cells. After electroporation, cells were plated on 4-6 18 mm glass coverslips coated with fibronectin (50 nM, Sigma) and equilibrated in culture medium. Cells were used one day after for transferrin uptake assay or imaging. Complete dynamin knock-out and dyn2-GFP re-expression was verified by Western Blot (WB) with a pan dynamin antibody (Santa Cruz sc-6401). Transfection efficiency was estimated by counting the cells with DAPI staining and the transfected cells with dyn2-GFP fluorescence. It was 46 ± 9 % in three separate experiments. Therefore, because the amount of expression of dyn2-GFP-WT in TKO cells estimated by WB was similar to the one in untreated (WT) cells (Figure 3B), we conclude that TKO cells transfected with dyn2-GFP-WT have about 2-fold overexpression of dynamin compared to WT cells. On the other hand, there was in the range of expression

bioRxiv preprint doi: https://doi.org/10.1101/309245; this version posted April 30, 2018. The copyright holder for this preprint (which was not certified by peer review) is the author/funder. All rights reserved. No reuse allowed without permission.

obtained here no correlation between the level of dyn2-GFP-WT and A568-Tfn uptake (Supplementary Figure 4B).

SK-MEL-2 cell clone Ti95 (Dnm2-GFP^{en} all edited) was a kind gift from David Drubin (University of California, Berkeley, CA). Cells were cultured in DMEM/F12 supplemented with 1% sodium pyruvate, 1% glutamax and 10% fetal calf serum (Invitrogen). Cells were plated on poly-L-lysine coated 18 mm glass coverslips and imaged the next day.

Live cell imaging

Imaging was performed at 34-37°C on an Olympus microscope (Olympus IX71 or IX83) equipped with an inverted Apochromat 60x oil objective of numerical aperture 1.49 in combination with a 1.6x magnifying lens; or with a 100x objective of numerical aperture 1.49 (Olympus). Samples were excited in TIRF illumination (Olympus IX2RFAEVA illuminator) with a 473 nm laser source (Cobolt). Emitted fluorescence was filtered with a 525/50m filter (Chroma Technology). Images were acquired by an electron multiplying charge coupled device camera (EMCCD QuantEM:512SC, Roper Scientific) controlled by the software MetaVue 7.8 (Molecular Devices). Two-colour imaging was performed with a co-aligned 561 nm laser (Cobolt) with the same TIRF angle as the 473 nm laser. Emitted fluorescence was filtered with a 605/52m filter (Chroma Technology). Red and green fluorescence images were obtained 200 ms apart using a filter wheel (Lambda 10-3, Sutter Instruments). To correct for x/y distortions between the two channels, images of fluorescently labelled beads (Tetraspeck, 0.2 µm; Invitrogen) were taken before each experiment and used to align the two channels. Time lapse images were acquired at 0.5 Hz with an integration time of 100 ms.

ppH assay Fast solution exchange was controlled by electro-valves (Lee company) connected to a theta glass pipette (TG150, Harvard Apparatus) pulled to ~100-µm tip size using a vertical puller (Narishige, World Precision Instruments) placed above the recorded cell. Cells were alternatively perfused with HEPES or MES buffered saline solutions (HBS/MBS) containing (in mM): 135 NaCl, 5 KCl, 0.4 $MgCl_2$, 1.8 $CaCl_2$, 1 D-glucose and 20 HEPES or MES. The pH was adjusted to 7.4 or 5.5 using NaOH and osmolarity to 310–315 mOsm.L^{-1} with NaCl.

Combined patch-clamp and imaging Cells were patched with pipettes made of borosilicate glass (GC150F, Harvard Apparatus) and pulled with a vertical Narishige puller (World Precision Instruments). The solution contained (in mM): 130-140 KCH_3SO_3, 1 EGTA, 0.1 $CaCl_2$, 10-20 HEPES, 4 ATP (sodium or magnesium salt), 0.4 Na-GTP (or GTPγS when indicated), 5

bioRxiv preprint doi: https://doi.org/10.1101/309245; this version posted April 30, 2018. The copyright holder for this preprint (which was not certified by peer review) is the author/funder. All rights reserved. No reuse allowed without permission.

phosphocreatine and 3 sodium ascorbate. pH was adjusted to 7.2 using KOH and osmolarity to ~300 mOsm.L^{-1}. Sodium ascorbate was omitted in earlier recordings but was added for better stability. Chloride ions either came from 2 mM KCl, 10 mM NaCl or 4 mM $MgCl_2$ (when Na-ATP was used) in various trials. All salts were purchased from Sigma-Aldrich. Cells were voltage-clamped at -60 mV with an EPC10 amplifier (HEKA) with series resistance and cell capacitance estimation every 4 s in the whole cell mode. The digital triggers of the amplifier were used to drive the electrovalves for pH changes. Cell viability and dialysis efficiency were made sure of by monitoring three parameters throughout the recording using the Patchmaster software (HEKA): series resistance should remain below 10 MΩ and holding current should remain above -100 pA. If either of these criteria was not respected (except holding current for recordings in GTPγS, see Supplementary Figure 3D), the recording was not considered for analysis. On a given experimental day at least one control recording (*i.e.* without any peptide) was performed to ensure recording quality. All these recordings were pooled in the 'control' condition (n = 63 on 42 experimental days). The nature of the peptide tested was unknown from the experimenter until the end of the recordings and analysis.

Image analysis and data representation

The detection, tracking, and quantification of endocytic events was performed using scripts developed previously and updated in Matlab 2017 (Mathworks)[15]. Images were sorted according to the pH (7.4 or 5.5) into two movies. These two movies were segmented using multidimensional image analysis (MIA; developed for Metamorph by JB Sibarita, Bordeaux, France) with fixed optimized parameters. Objects appearing in pH 5.5 images were then considered *candidate* CCVs if they were visible for more than 3 frames (8 to 12 s), if their signal to noise ratio was high enough, and if a cluster pre-existed where they appeared for at least 5 frames (20 to 24 s) in pH 7.4 images (Supplementary Figure 2B). Importantly, this automated method of detection had been characterised as missing ~30% of all events but with a low percentage of false positives (~20%)[15,17], making it ideal for comparative studies over large datasets. However, to estimate better the inhibition by peptides, we wanted to make sure that the degree of false positives were kept as low as possible without reviewing all the events by eye. We thus developed a Support Vector Machine (SVM) type neural network by supervised learning. We used a dataset of 26 recordings obtained in 6 experimental sessions with 9631 candidate events reviewed by two different operators (MR and DP), leading to 7763

bioRxiv preprint doi: https://doi.org/10.1101/309245; this version posted April 30, 2018. The copyright holder for this preprint (which was not certified by peer review) is the author/funder. All rights reserved. No reuse allowed without permission.

bona fide endocytic events. This gives 19.1 ± 0.1 % of false positives, a percentage virtually identical to previous estimates[15,17]. The inputs of the SVM were sets of 15x15 pixel images centred on the candidate event, 5 frames before and 6 frames after the candidate event is detected, i.e. 15x15x11 = 2475 input values (pixel values) per candidate event. The output was binary, 'accepted' or 'rejected' (Supplementary Figure 2C,D). Once trained, the SVM model could sort correctly all events used for training. We tested it further with 7 recordings with 1224 candidate events sorted by the user in 1124 *bona fide* events. The SVM sorted 1095 *bona fide* events (98.4 ± 2.0 % of the number of events accepted by the user). Finally 93.5 ± 1.1 % were the same as the events accepted by the users. We conclude from this analysis that the SVM trained by the 26 recordings is able to discriminate *bona fide* events with the same accuracy as a human operator, and probably with better consistency. In conclusion, we developed a fully automated analysis workflow to assess quantitatively the endocytic activity of cells in real time.

The cumulative frequency plots presented in Figure 2B,C were obtained by plotting event detections against time. For each recording, the frequency of events in both cell attached and whole cell recordings were normalised to the basal frequency of the cell as monitored in cell attached configuration. In other words, the curves were normalised so that the number of detections at the 70th frame of cell attached recording (280 s) would be set to 100. In this way, several cells submitted to the same treatment could be pooled into a single curve despite a great variability in their basal endocytic activity. The effect of a blocker was then measured as

$$\left(\frac{F_{WC}([8-10])}{F_{CA}([2-4])}\right) * 100$$

where F is the frequency of events in the indicated time interval (in minutes) and the subscript is the recording mode in which it is being measured (CA: cell attached, WC: whole cell).

The recruitment of dyn2-GFP was analysed by segmentation and tracking as for TfR-SEP recordings. Objects that could be tracked for more than 3 frames (6 s) were retained for further analysis. The fluorescence value at each time point represents the average intensity in a 2 pixel (300 nm) radius circle around the centre of mass of the object to which the local background intensity is subtracted. This local background is estimated in an annulus (5 pixels outer radius, 2 pixels inner radius) centred on the region to be quantified as the average

bioRxiv preprint doi: https://doi.org/10.1101/309245; this version posted April 30, 2018. The copyright holder for this preprint (which was not certified by peer review) is the author/funder. All rights reserved. No reuse allowed without permission.

intensity of pixel values between the 20th and 80th percentiles (to exclude neighbouring fluorescent objects). The frame of maximum intensity is used as the reference (time 0) for aligning and averaging all traces. Before (resp. after) tracking of an object the fluorescence is measured at the location of the first (resp. last) frame with the object tracked. The quantification of TfR-SEP (at pH 7.4 and 5.5) and dyn2-mCherry was performed as in in the same manner using the coordinates of TfR-SEP at pH 5.5 (vesicles) and explained in detail in [15]. Briefly, two colour alignment was performed using the bead image taken before the experiment. Correction for bleed through was performed by minimizing the difference between the dyn2-mCherry fluorescence values at the two pH with a green to red bleed through factor. Finally, 95% confidence intervals for significant recruitment were obtained by shifting the real event coordinates within the cell mask 200 times and computed fluorescence on these shifted coordinates.

Transferrin uptake assay and quantification

TKO cells were starved in pre-warmed HBS for 10 min, then incubated in cold (4 °C) HBS containing 10 µg/ml of transferrin Alexa 568 (Tfn-A568, Thermo Fischer). Cells were then incubated at 37 °C for 5 min for endocytosis to occur. Afterwards, cells were washed in cold HBS, then in cold acetate buffer (pH 4.5) for 2 min to strip Tfn-A568 remaining on the cell surface, rinsed, and fixed with paraformaldehyde (4% in PBS, 37 °C) for 15 minutes. Cells were then rinsed several times in PBS and kept at 4°C until imaging. Fixed cells were then imaged with a spinning disk confocal microscope with a stack of 6 images separated by 0.5 µm encompassing the bottom part adhering to the coverslip with laser and camera parameters kept constant for the whole set of conditions. We used the maximal projection of the z-stack for quantification. For each cell, we traced around the dyn-GFP image (when applicable) a mask of the cell, as well as a background region with no cell. In non-transfected the mask was traced around the Tfn-A568 image. We detected Tfn-A568 clusters by wavelet segmentation. For each cell we computed the average fluorescence, the number of clusters and the cell surface. These numbers were normalized to 100 for the control condition (no OHT induction) for each of four independent internalization assays. The distribution of dyn-GFP was scored for each cell as entirely punctuate (1), punctuate on a homogenous background (2), mostly homogenous with some puncta (3), or entirely homogenous (4)(see Figure 3F for illustrations). All data processing and scoring was performed blind.

bioRxiv preprint doi: https://doi.org/10.1101/309245; this version posted April 30, 2018. The copyright holder for this preprint (which was not certified by peer review) is the author/funder. All rights reserved. No reuse allowed without permission.

Statistical analysis

Data is presented as average ± SEM unless otherwise stated. Differences between conditions were tested by a one way ANOVA followed by Tukey's multiple comparison tests. Dyn2-GFP localization scores were compared with Kruskall-Wallis non parametric test followed by Dunn's multiple comparison tests. Variations of C_m during whole cell recordings were tested with Student's paired T tests. All values were calculated with Prism 7 (Graphpad). P values are displayed in the Supplementary Table 3.

bioRxiv preprint doi: https://doi.org/10.1101/309245; this version posted April 30, 2018. The copyright holder for this preprint (which was not certified by peer review) is the author/funder. All rights reserved. No reuse allowed without permission.

Inventory of Supplementary Data

Supplementary Figure 1: Synthesis and characterization of divalent peptides

Supplementary Figure 2: Workflow of automated analysis of ppH data (SVM for final validation)

Supplementary Figure 3: Characteristics of the whole cell recordings in the different conditions of this study.

Supplementary Figure 4: The degree of expression of dynamin mutants does not correlate with internalized transferrin.

Supplementary Table 1: characteristics of the divalent peptides

Supplementary Table 2: Proteins identified by mass spectrometry after dD15-N pull down

Supplementary Table 3: P values for the statistical tests used in Figures 2 and 3.

bioRxiv preprint doi: https://doi.org/10.1101/309245; this version posted April 30, 2018. The copyright holder for this preprint (which was not certified by peer review) is the author/funder. All rights reserved. No reuse allowed without permission.

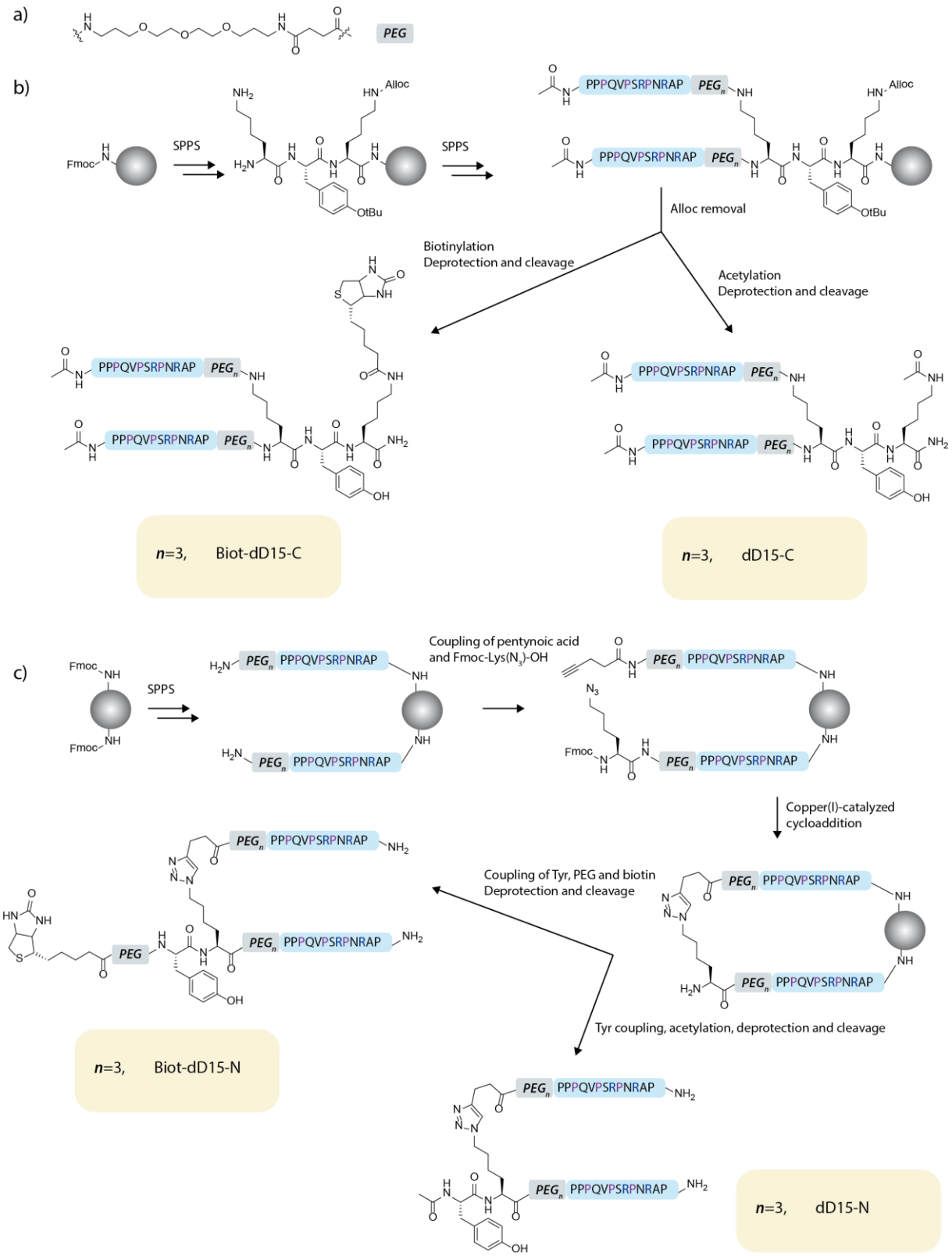

Supplementary Figure 1: Synthesis and structure of the divalent peptides. a) Chemical structure of the PEG residue. b) Synthetic schemes and structure of the C-terminally linked divalent peptides. c) Synthetic schemes and structure of the N-terminally linked divalent peptides.

bioRxiv preprint doi: https://doi.org/10.1101/309245; this version posted April 30, 2018. The copyright holder for this preprint (which was not certified by peer review) is the author/funder. All rights reserved. No reuse allowed without permission.

Name	Sequence	Formula	Mass (m/z) [a]		Rt (min), [purity] [b]
			Expected M	Obtained [M+H] [a]	
Ac-D15	Ac-YPPPQVPSRPNRAPPG-$CONH_2$	$C_{80}H_{123}N_{25}O_{21}$	1769,9	1771,0	20.8 [93%]
Biot-D15	Biot-PEG-YPPPQVPSRPNRAPPG-$CONH_2$	$C_{102}H_{161}N_{29}O_{27}S$	2256,2	2257,2	ND
Ac-D44	Ac-YALGGAPPVPSRPGASPDPFGPPPQVPSRPNRAPPGVPRITISDP-$CONH_2$	$C_{207}H_{322}N_{60}O_{58}$	4576,4	4576,3	26.1 []
Biot-D44	Biot-PEG-YALGGAPPVPSRPGASPDPFGPPPQVPSRPNRAPPGVPRITISDP-$CONH_2$	$C_{229}H_{360}N_{64}O_{64}S$	5062,7	5062,5	ND
Ac-N-D30	Ac-YPPVPSRPGASPDPFGPPPQVPSRPNRAPPG-$CONH_2$	$C_{147}H_{221}N_{43}O_{40}$	3228,7	3229,3	24.4 [92%]
dD15-N		$C_{249}H_{418}N_{64}O_{73}$	5473,1	5471,2	24.5 [93%]
Biot-dD15-N		$C_{257}H_{430}N_{66}O_{74}S$	5657,2	5658,4	24.9 [92%]
dD15-C		$C_{244}H_{405}N_{65}O_{71}$	5382,0	5385,1	24.8 [85%]
Biot-dD15-C		$C_{266}H_{443}N_{69}O_{77}S$	5868,3	5868,1	24.7 [87%]

Supplementary Table 1: Characterization of the synthetized peptides used in this study

bioRxiv preprint doi: https://doi.org/10.1101/309245; this version posted April 30, 2018. The copyright holder for this preprint (which was not certified by peer review) is the author/funder. All rights reserved. No reuse allowed without permission.

Supplementary Table 3: Proteomics analysis of the proteins interacting with dD15-N.

Name	#SH3 domain	BAR domain	Peptide count	Unique peptides	Confidence score	ANOVA (p)	Max fold change	Description	Accession
SH3 domain-containing proteins (known Dynamin partners)									
SH3kbp1	3	NO	89	84	264.8	1.2E-04	207.5	SH3 domain-containing kinase-binding protein 1 OS=Rattus norvegicus GN=Sh3kbp1 PE=1 SV=2 - [SH3K1_RAT]	Q925Q9;A0A0H2UHD8;M0RBZ7
Intersectin-2	5	NO	85	82	245.0	2.6E-04	118.9	Intersectin 2 OS=Rattus norvegicus GN=Itsn2 PE=1 SV=2 - [M0R7A6_RAT]	M0R7A6
Intersectin-1	5	NO	20	17	52.3	1.3E-05	60.7	Intersectin-1 OS=Rattus norvegicus GN=Itsn1 PE=1 SV=3 - [D3ZV52_RAT]	D3ZV52;F1M823;Q9WVE9
Amph1	1	YES	20	19	49.2	2.8E-04	40.7	Amphiphysin OS=Rattus norvegicus GN=Amph PE=1 SV=1 - [AMPH_RAT]	O08838;A0A0G2JX32;A0A0G2K5Z4;F1LPP0;Q68FR2
Bin1 (Amph2)	1	YES	18	17	42.0	1.1E-03	70.2	Myc box-dependent-interacting protein 1 OS=Rattus norvegicus GN=Bin1 PE=1 SV=1 - [BIN1_RAT]	O08839;D4A4P1;F1LMX1;Q5HZA7
Endophilin-A1	1	YES	9	6	22.7	4.7E-03	53.5	Endophilin-A1 OS=Rattus norvegicus GN=Sh3gl2 PE=1 SV=2 - [SH3G2_RAT]	O35179
Snx18	1	NO	5	5	10.2	2.9E-04	16.1	Sorting nexin OS=Rattus norvegicus GN=Snx18 PE=1 SV=1 - [D3ZZ38_RAT]	D3ZZ38
Endophilin-A2	1	YES	5	2	10.1	2.8E-03	1.7	Endophilin-A2 OS=Rattus norvegicus GN=Sh3gl1 PE=1 SV=1 - [SH3G1_RAT]	O35964
SH3 domain-containing proteins (other)									
CD2-ap	3	NO	52	51	125.5	8.5E-06	124.5	CD2-associated protein OS=Rattus norvegicus GN=Cd2ap PE=1 SV=2 - [CD2AP_RAT]	F1LRS8
SH3d19	4	NO	22	22	55.7	1.5E-03	42.9	SH3 domain-containing 19 OS=Rattus norvegicus GN=Sh3d19 PE=1 SV=1 - [D3Z8S0_RAT]	D3Z8S0;D3ZV20
CCP-related proteins									
Eps15l1	0	NO	92	92	252.9	1.5E-05	196.9	Epidermal growth factor receptor pathway substrate 15-like 1 OS=Rattus norvegicus GN=Eps15l1 PE=1 SV=3 - [D3ZJR1_RAT]	D3ZJR1
Hspa8	0	NO	23	20	62.0	7.8E-03	15.6	Heat shock cognate 71 kDa protein OS=Rattus norvegicus GN=Hspa8 PE=3 SV=3 - [D4A4S3_RAT]	D4A4S3;A0A0G2JUT0;A0A0G2JVI3;F1LZI1;M0R8M9;M0RCB1;P0DMW0;P14659;P55063;P63018
CHC	0	NO	25	25	59.5	1.3E-04	22.7	Clathrin heavy chain OS=Rattus norvegicus GN=Cltc PE=1 SV=1 - [F1M779_RAT]	F1M779;P11442
AP2a1	0	NO	24	18	56.2	2.1E-05	28.6	AP-2 complex subunit alpha OS=Rattus norvegicus GN=Ap2a1 PE=1 SV=1 - [D3ZUY8_RAT]	D3ZUY8
AP2a2	0	NO	22	16	50.3	1.3E-03	13.8	AP-2 complex subunit alpha OS=Rattus norvegicus GN=Ap2a2 PE=1 SV=1 - [Q66HM2_RAT]	Q66HM2;A0A0G2K943;P18484
AP2b1	0	NO	17	17	40.9	5.4E-07	40.0	AP-2 complex subunit beta OS=Rattus norvegicus GN=Ap2b1 PE=1 SV=1 - [AP2B1_RAT]	P62944;A0A0G2K2V2;G3V9N8;P52303
AP2m1	0	NO	7	7	15.4	9.4E-04	25.5	AP-2 complex subunit mu OS=Rattus norvegicus GN=Ap2m1 PE=1 SV=1 - [A0A140TAH5_RAT]	A0A140TAH5;P84092
Dnm1	0	NO	2	2	4.9	1.1E-02	27.4	Dynamin-1 OS=Rattus norvegicus GN=Dnm1 PE=1 SV=2 - [DYN1_RAT]	P21575;A0A0A0MY48;A0A0A0MY49;P39052
Cytoskeleton proteins									
Actg1	0	NO	13	5	36.3	2.1E-01	2.2	Actin, cytoplasmic 2 OS=Rattus norvegicus GN=Actg1 PE=1 SV=1 - [ACTG_RAT]	P63259;A0A0G2K3K2;P60711
Tubb3	0	NO	14	2	30.9	3.8E-01	1.2	Tubulin beta-3 chain OS=Rattus norvegicus GN=Tubb3 PE=1 SV=1 - [TBB3_RAT]	Q4QRB4;M0R8B6
Tubb4a	0	NO	13	2	30.1	6.6E-03	43.4	Tubulin beta chain OS=Rattus norvegicus GN=Tubb4a PE=1 SV=1 - [B4F7C2_RAT]	B4F7C2
Tubb5	0	NO	11	2	28.9	2.5E-03	18.0	Tubulin beta-5 chain OS=Rattus norvegicus GN=Tubb5 PE=1 SV=1 - [TBB5_RAT]	P69897
Tubb2a	0	NO	12	3	28.3	1.6E-03	75.4	Tubulin beta-2A chain OS=Rattus norvegicus GN=Tubb2a PE=1 SV=1 - [TBB2A_RAT]	P85108;Q3KRE8
Tuba1a	0	NO	11	4	26.4	1.5E-02	13.3	Tubulin alpha-1A chain OS=Rattus norvegicus GN=Tuba1a PE=1 SV=1 - [TBA1A_RAT]	P68370;A0A0H2UHM7;F1LUM5;Q68FR8;Q6AY56;Q6AYZ1;Q6P9V9
Actg2	0	NO	9	2	22.7	3.2E-01	2.3	Actin, gamma-enteric smooth muscle OS=Rattus norvegicus GN=Actg2 PE=2 SV=1 - [ACTH_RAT]	P63269;A0A0G2K4M6;P62738;P68035;P68136
Tuba4a	0	NO	10	3	20.3	1.4E-02	14.5	Tubulin alpha-4A chain OS=Rattus norvegicus GN=Tuba4a PE=1 SV=1 - [TBA4A_RAT]	Q5XIF6
Capza1	0	NO	3	2	6.3	3.9E-02	23.0	F-actin-capping protein subunit alpha-1 OS=Rattus norvegicus GN=Capza1 PE=1 SV=1 - [CAZA1_RAT]	B2GUZ5
Other proteins									
Calcoco1	0	NO	16	16	38.3	2.4E-03	11.9	Calcium-binding and coiled-coil domain-containing protein 1 OS=Rattus norvegicus GN=Calcoco1 PE=2 SV=1 - [CACO1_RAT]	Q66HR5;A0A0G2K0S1;A0A1B0GWP3
Hspa5	0	NO	11	8	30.1	3.8E-02	4.1	78 kDa glucose-regulated protein OS=Rattus norvegicus GN=Hspa5 PE=1 SV=1 - [GRP78_RAT]	P06761
Rundc3a	0	NO	7	7	20.0	5.9E-04	16.0	RUN domain-containing 3A OS=Rattus norvegicus GN=Rundc3a PE=1 SV=1 - [F1LRZ9_RAT]	F1LRZ9
Hspa9	0	NO	7	6	17.2	3.2E-04	42.1	Stress-70 protein, mitochondrial OS=Rattus norvegicus GN=Hspa9 PE=1 SV=3 - [GRP75_RAT]	P48721;F1M953
Amy1a	0	NO	6	6	14.4	1.4E-01	2.8	Alpha-amylase OS=Rattus norvegicus GN=Amy1a PE=1 SV=3 - [E9PSQ1_RAT]	E9PSQ1;A0A0G2K6T1;E9PSI7;G3V844;P00689
Atp1a3	0	NO	3	3	6.0	1.6E-03	33.4	Sodium/potassium-transporting ATPase subunit alpha-3 OS=Rattus norvegicus GN=Atp1a3 PE=1 SV=2 - [AT1A3_RAT]	P06687;P06685;P06686
Ubc	0	NO	2	2	5.9	5.5E-01	1.2	Polyubiquitin-C OS=Rattus norvegicus GN=Ubc PE=1 SV=1 - [UBC_RAT]	Q63429;F1LML2;F1LU69;F1M927;P0CG51;P62982;P62986
Appbp2	0	NO	3	3	4.8	7.3E-04	20.8	Amyloid protein-binding protein 2 OS=Rattus norvegicus GN=Appbp2 PE=2 SV=1 - [APBP2_RAT]	A5HK05

bioRxiv preprint doi: https://doi.org/10.1101/309245; this version posted April 30, 2018. The copyright holder for this preprint (which was not certified by peer review) is the author/funder. All rights reserved. No reuse allowed without permission.

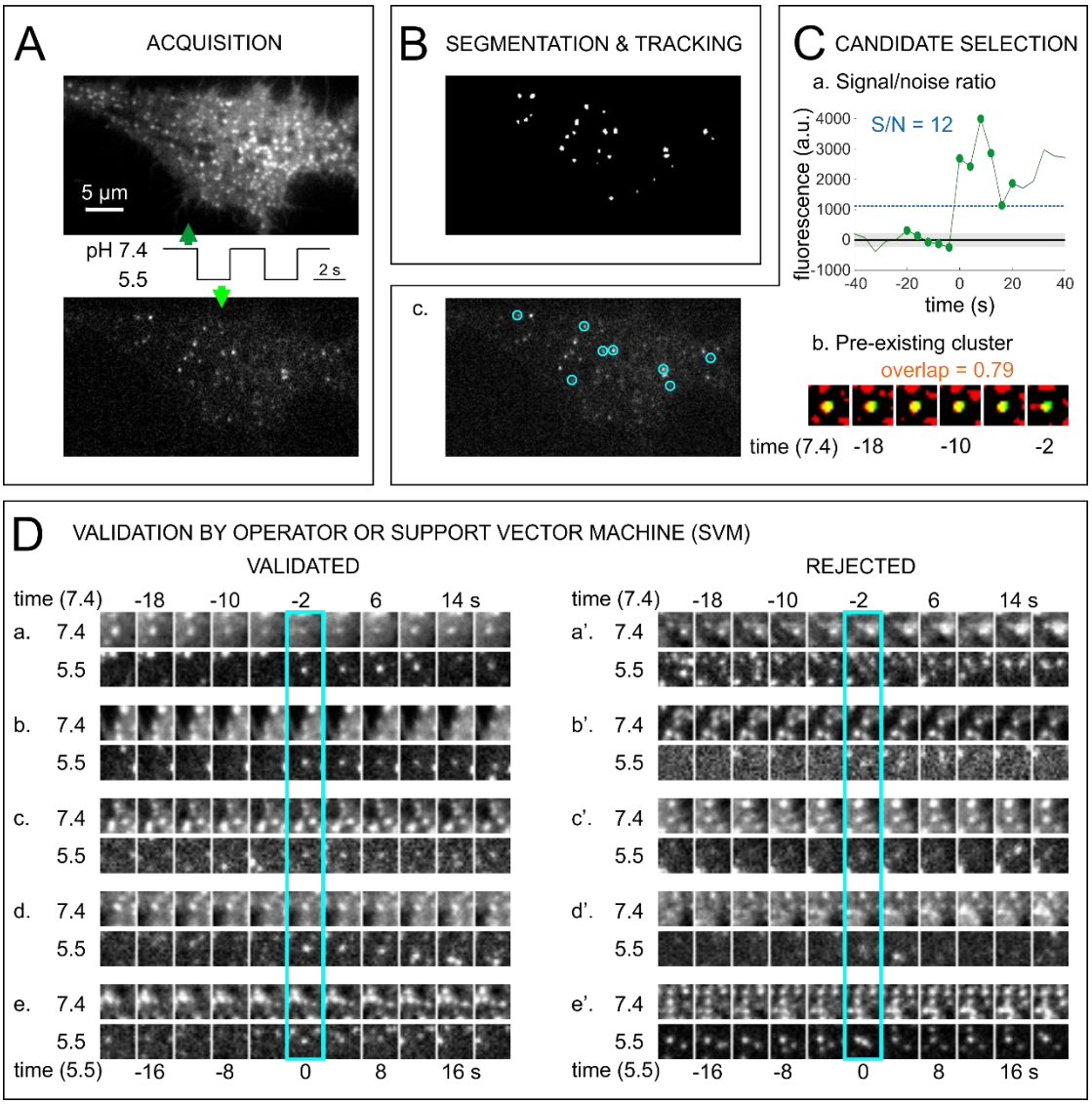

Supplementary Figure 2: **Workflow of automated analysis of ppH data.** The four steps (A-D) leading to the characterization of scission events. **A**, Acquisition of images alternatively at pH 7.4 and pH 5.5. Two consecutive images are shown. The image at pH 5.5 is shown with 8x higher brightness than the one at pH 7.4. **B**, Segmentation and tracking of clusters visible at pH 5.5 on the image shown in A. **C**, Selection of candidate events based on two criteria. a. Signal/noise ratio. The average fluorescence in a circle of 2 pixels radius centered on the center of mass of the segmented object is plotted for each frame before and at the start of segmentation (time 0). The noise is estimated as the average ± std before detection (black line, average; gray shading, std). An event is qualified as candidate if the fluorescence at detection divided by the noise estimate (S/N) is bigger than 5. The example (corresponding to event a. in panel D) has S/N = 12.0. b. Pre-existing cluster at pH 7.4. In segmented images, the location of the event (green) is compared to the clusters of TfR visible at pH 7.4 (red) for the five frames preceding the event. The fraction of green pixels overlapping with red (appearing in yellow) gives an estimate of the colocalization of the candidate vesicle with a parent cluster. An event is qualified as candidate when this fraction is greater than 0.2. For the displayed example (event a. in Panel D) the fraction overlap is 0.79. c. The cyan circles mark the clusters segmented in B which passed the criteria. **D**, Final event validation by a human operator or

bioRxiv preprint doi: https://doi.org/10.1101/309245; this version posted April 30, 2018. The copyright holder for this preprint (which was not certified by peer review) is the author/funder. All rights reserved. No reuse allowed without permission.

the trained SVM. Left, gallery of events which were validated by a human operator. In all cases (a-e) the acid resistant spot (vesicle) is clearly visible and can be tracked. Right, gallery of events which were selected by the first screen described in C but subsequently rejected by a human operator. In cases a', d' and e' the acid resistant spot cannot be tracked consistently and in cases b' and c' it is barely above background. The choices made for validation and rejection, together with 9621 others, have served to train the SVM.

bioRxiv preprint doi: https://doi.org/10.1101/309245; this version posted April 30, 2018. The copyright holder for this preprint (which was not certified by peer review) is the author/funder. All rights reserved. No reuse allowed without permission.

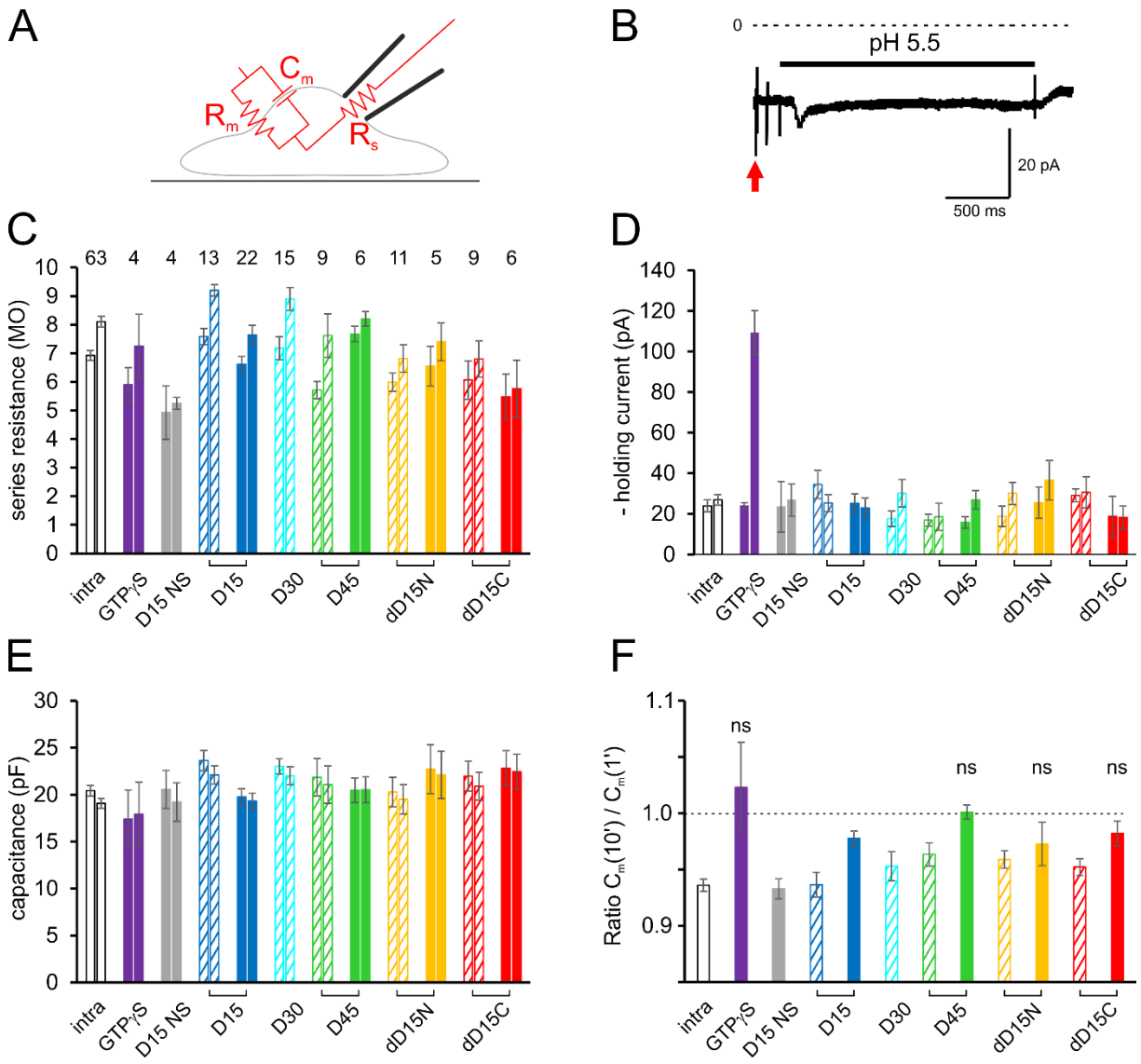

Supplementary Figure 3: Characteristics of the whole cell recordings in the different conditions of this study. A, Scheme of the equivalent electrical circuit of a cell recorded in the whole cell configuration. The electrical circuit in *red* is estimated by a voltage pulse (*red arrow* in B) and compensated by the patch clamp amplifier. Series resistance (R_s) depends on the pipette resistance and the access to the cell cytoplasm. It reflects the ability of the pipette solution containing the blocking peptides to diffuse into the cell. Membrane capacitance (C_m) is proportional to the plasma membrane surface. Membrane resistance (R_m) is inversely proportional to the number of open channels. **B**, Example of a current recording of a cell held in voltage clamp at -60 mV. The holding current is -21 pA. The application of solution at pH 5.5 evokes a current of less than 5 pA. Fast transient currents reflect the response to the test voltage step (*red arrow*, -5 mV, 10 ms, see A) and the electrical artefacts of electro-valve openings to exchange the extracellular solutions. **C**, Series resistance R_s for each recording condition (same cells as in Figure 2D), during the 1st minute (left) and the 10th minute (right) of whole cell recording. R_s were maintained below 10 MΩ throughout the recording and do not differ between conditions as compared to the control condition (one way ANOVA and Tukey multiple comparison tests). **D**, Same as C for holding current. There was no significant difference between conditions (one way ANOVA and Tukey's multiple comparison tests)

bioRxiv preprint doi: https://doi.org/10.1101/309245; this version posted April 30, 2018. The copyright holder for this preprint (which was not certified by peer review) is the author/funder. All rights reserved. No reuse allowed without permission.

except for GTPγS at the 10th minute where the holding current was much larger ($p < 0.0001$). This is likely due to the activation of GTP dependent trimeric G proteins which activate various channels in the presence of GTPγS, thereby increasing the holding current. **E**, Same as C for membrane capacitance C_m. There were no differences between conditions (one way ANOVA and Tukey multiple comparison tests). **F**, Ratios of C_m recorded during the 10th minute of recording over C_m recorded during the 1st minute. The variation in C_m indicates the balance between exocytosis and endocytosis. In control conditions, the relative membrane capacitance slightly but significant decreases: $C_m(10')/C_m(1') = 0.936 \pm 0.006$ ($p < 10^{-13}$ paired t-test). If endocytosis is blocked, C_m would be expected to stop decreasing or even increase. In four conditions (GTPγS, D44 1 mM, dD15-N 1mM, dD15-C 1 mM) there was no significant decrease in C_m ($p = 0.49$; 0.67; 0.27; 0.14, respectively). These four conditions correspond to the strongest decrease in endocytic event frequency measured with the ppH assay (see Figure 2D). All graphs indicate average ± SEM.

bioRxiv preprint doi: https://doi.org/10.1101/309245; this version posted April 30, 2018. The copyright holder for this preprint (which was not certified by peer review) is the author/funder. All rights reserved. No reuse allowed without permission.

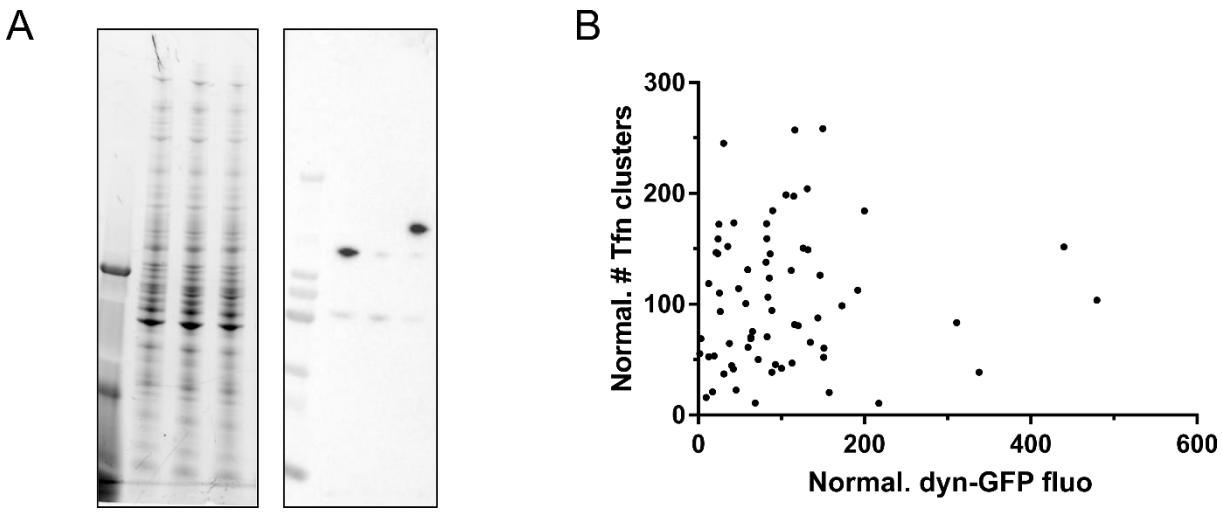

Supplementary Figure 4: The degree of expression of dynamin mutants does not correlate with internalized transferrin. A, Full blots corresponding to Figure 3B. Left, stain free detection of total protein. Lane 1, size markers; lanes 2-4, untreated, treated with OHT, treated with OHT and transfected with dyn2-GFP-WT, respectively. Right, blot corresponding with anti-dynamin antibody. **B**, The fluorescence of each TKO cell transfected with dyn2-GFP-WT was measured as the average in the mask normalized to 100 for each of four experimental session. There was no significant correlation between the two parameters (Pearson r = 0.058; p = 0.64)

bioRxiv preprint doi: https://doi.org/10.1101/309245; this version posted April 30, 2018. The copyright holder for this preprint (which was not certified by peer review) is the author/funder. All rights reserved. No reuse allowed without permission.

Supplementary Table 3: p-values for 1-way ANOVA followed by Tukey's multiple comparison tests

1. Effect of peptides on endocytic event frequency (Figure 2D)

Comparison Control WC vs.		
No WC recording	ns	0.5799
GTPγS	**	0.0012
D15 NS 1 mM	ns	>0.9999
D15 0.1 mM	ns	0.9878
D15 1 mM	***	0.0002
D30 0.1 mM	*	0.0338
D44 0.1 mM	*	0.0359
D44 1 mM	****	< 0.0001
dD15-N 0.1 mM	*	0.0476
dD15-N 1 mM	*	0.0132
dD15-C 0.1 mM	*	0.0339
dD15-C 1 mM	****	< 0.0001

2. Tfn-A568 uptake assays (Figure 3E)

Comparison No treatment vs.			Comparison OHT only vs.		
OHT only	****	< 0.0001	No treatment	****	< 0.0001
OHT and dyn2-GFP-WT	ns	>0.9999	OHT and dyn2-GFP-WT	****	< 0.0001
OHT and dyn2-GFP-ΔPRD	****	< 0.0001	OHT and dyn2-GFP-ΔPRD	ns	0.9893
OHT and dyn2-GFP-ΔCter	****	< 0.0001	OHT and dyn2-GFP-ΔCter	ns	0.2156
OHT and dyn2-GFP-ABC_{mut}	****	< 0.0001	OHT and dyn2-GFP-ABC_{mut}	ns	0.9751
OHT and dyn2-GFP-A_{mut}	ns	0.9997	OHT and dyn2-GFP-A_{mut}	****	< 0.0001
OHT and dyn2-GFP-B_{mut}	****	< 0.0001	OHT and dyn2-GFP-B_{mut}	****	< 0.0001
OHT and dyn2-GFP-C_{mut}	***	0.0001	OHT and dyn2-GFP-C_{mut}	****	< 0.0001
OHT and dyn2-GFP-AC_{mut}	****	< 0.0001	OHT and dyn2-GFP-AC_{mut}	*	0.0411

3. Dyn2-GFP localisation in TKO cells (Figure 3F)

Comparison dyn2-GFP-WT vs.			Comparison dyn2-GFP-ΔPRD vs.		
dyn2-GFP-ΔPRD	****	< 0.0001	dyn2-GFP-WT	****	< 0.0001
dyn2-GFP-ΔCter	****	< 0.0001	dyn2-GFP-ΔCter	ns	>0.9999
dyn2-GFP-ABC_{mut}	****	< 0.0001	dyn2-GFP-ABC_{mut}	ns	>0.9999
dyn2-GFP-A_{mut}	ns	>0.9999	dyn2-GFP-A_{mut}	****	< 0.0001
dyn2-GFP-B_{mut}	****	< 0.0001	dyn2-GFP-B_{mut}	****	< 0.0001
dyn2-GFP-C_{mut}	***	0.0001	dyn2-GFP-C_{mut}	****	< 0.0001
dyn2-GFP-AC_{mut}	****	< 0.0001	dyn2-GFP-AC_{mut}	*	0.0117